Nearshore submerged wave farm optimisation

A multi-objective approach

David, Daniel R.; Kurniawan, Adi; Wolgamot, Hugh; Hansen, Jeff E.; Rijnsdorp, Dirk; Lowe, Ryan

DOI
10.1016/j.apor.2022.103225

Publication date
2022

Document Version
Final published version

Published in
Applied Ocean Research

Applied Ocean Research 124 (2022) 103225

Contents lists available at ScienceDirect

Applied Ocean Research

journal homepage: www.elsevier.com/locate/apor

Nearshore submerged wave farm optimisation: A multi-objective approach

Daniel R. David [a,b,c,*], Adi Kurniawan [b,d], Hugh Wolgamot [b,c,d], Jeff E. Hansen [a,b,c], Dirk Rijnsdorp [b,d,e], Ryan Lowe [a,b,c,d]

[a] School of Earth Sciences, The University of Western Australia, Australia
[b] Marine Energy Research Australia, The University of Western Australia, Australia
[c] UWA Oceans Institute, The University of Western Australia, Australia
[d] Oceans Graduate School, The University of Western Australia, Australia
[e] Delft University of Technology, Delft, the Netherlands

ARTICLE INFO

Keywords:
Wave farms
Wave energy converters
Multi-objective optimisation
Wave power
LCoE
Loads

ABSTRACT

To be commercially viable, wave energy converters (WECs) will need to be deployed in arrays or "wave farms" to generate significant amounts of energy and to have the costs of these farms minimised. However, when designing a wave farm, there are a number of trade-offs to be made between competing objectives; for example, between the power production potential and installation costs, with the optimal design for one objective not necessarily favourable for the other. In this study, we developed a multi-objective optimisation methodology to allow rigorous evaluation of the trade-offs amongst multiple objectives. We demonstrate the methodology for four objectives: (1) maximising power production, (2) minimising the foundation loads, (3) minimising the number of foundations and (4) minimising the total export cable length required. However, the method is flexible and can be used for optimising a range of other parameters. A case study examining multi-objective optimisation of a wave farm using the developed probability-based evolutionary strategy was conducted for a proposed development site in Albany, Western Australia. The wave farms were composed of 5, 10 and 20 fully submerged cylindrical point-absorber type WECs similar to Carnegie Clean Energy's CETO-6 device. Simulations show that the optimal layouts preferring maximum power formed a single line perpendicular to the predominant wave direction; the optimal layouts preferring minimum cable length and a minimum number of foundations form multiple lines; whereas the optimal layouts preferring minimum foundation loads formed multiple lines in line with the predominant wave direction. By applying a cost model and non-dominated sorting, the methodology allowed us to quantify the trade-offs between power production and cost.

1. Introduction

Global energy demand is predicted to increase by a further 25% by 2040 compared to 2017 (Ghasemian et al., 2020). To satisfy this demand, while also reducing carbon emissions, renewable energy technologies will become increasingly important to the global energy mix. Due to the high energy density of ocean waves, and their consistency, wave energy technology has drawn increased attention. As a result, several wave energy technologies have been developed over the years. Regardless of the category, all wave energy converters (WECs) will have to be deployed in arrays or "wave farms" to generate electricity on a commercial scale.

Several theoretical studies considering regular waves (e.g., Budal 1977, Evans 1980, Falnes 1980, Thomas and Evans 1981) have shown that, for certain wave frequencies, the power generated by an array can be more than that from the same number of WECs in isolation (quantified by the interaction factor, q (Budal, 1977), which is > 1 for positive interactions). Conversely, the opposite ($q < 1$) can occur for other wave frequencies, causing the array power to be lower than the power from the same number of isolated WECs. These responses are due to regions of constructive and destructive interactions within WEC arrays. To understand how constructive and destructive interactions can impact the power generated by arrays, numerous studies have focussed on array interactions with different farm parameters such as inter-WEC spacing, wave direction, number of WECs in the array, or a combination of these (e.g., Babarit 2013, Fitzgerald and Thomas 2016, McIver 1994, Wolgamot et al. 2012, Zhong and Yeung 2019). Although it is beneficial to achieve optimum power generation by exploiting constructive interactions within the array, this is sometimes beyond the capabilities of

* Corresponding author at: School of Earth Sciences, The University of Western Australia, Australia.
E-mail address: daniel.david@research.uwa.edu.au (D.R. David).

https://doi.org/10.1016/j.apor.2022.103225
Received 29 December 2021; Received in revised form 23 May 2022; Accepted 29 May 2022
Available online 3 June 2022

Nomenclature

Term/Notation	Definition
A	incident wave amplitude
$\boldsymbol{A_m}$	added mass matrix
b_{pto}	damping coefficients
$\boldsymbol{B}$	matrix of radiation damping coefficients
$\boldsymbol{B_{pto}}$	damping coefficient matrix
BA	buoyant actuator
c	mutation coefficient
C	cluster
$cost_f$	foundation cost
$cost_{pi}$	pile installation cost
$cost_{pm}$	pile manufacturing cost
$cost_{st}$	steel unit cost
$cost_{\text{vessel}}$	vessel operation day cost
D	diameter of Buoyant Actuator
d_c	distance between clusters
E	undirected weighted graph edges
$\boldsymbol{f}$	objective functions
$\widehat{\mathbf{F}}_{\mathbf{e}}$	vector of complex excitation forces
$f_k(\vartheta^i)$	map of the decision variable (ϑ) i
$f_k^{\max}$	maximum function values
$f_k^{\min}$	minimum function values
$F_{l,n}$	load transfer function ($n = 1,2,3$)
G	cost metric
G^n	normalized cost
GA	genetic algorithm
GAM	grid array model
h	depth below seabed
h_t	height above pile tip
H_s	significant wave height
i	imaginary unit
J	iteration number
$\widehat{k}$	unit vector in the vertical direction
k_{pto}	spring coefficients
$\boldsymbol{K_{pto}}$	spring coefficient matrix
L	total number of sea states
LAM	linear array model
L_c	cable length
ls	least square
ls normal	line normal to least square axis
LCoE	levelized Cost of Energy
$\boldsymbol{M}$	mass matrix
M_d	distance between foundations
MOEA	evolutionary multi-objective optimisation
n	number of objective functions
N	total number of WECs
N_a	number of anchors
N_a^n	normalised number of anchors
N_{blow}	number of driving blows for per metre penetration
N_c	number of cycles
O_l	probability of occurrence of the l^{th} sea state
PopSize	population size
P	time-averaged power
P_{cons}	mean power absorbed in constrained case
P_{uncons}	mean power absorbed in the unconstrained case
P_D	pile diameter
P_{Di}	inner diameter of the pile
P_{iso}	isolated WEC power
P_l	power absorbed in the l^{th} sea state
P_L	pile length
P_{max}	maximum power
P_{mean}	mean Power
$P(R)$	long term probability not exceeding the return load R
PTO	power take-off
q	interaction factor
q_c	cone tip resistance profile
Q	probability level
r_k	number of rows in an array 'k' (*LAM*)
$r_{\max}$	pre-selected radius
R	return load
R_{20}	20-year return load
$R_{20,cons}$	20-year return load in constrained case
$R_{20,uncons}$	20-year return load in the unconstrained case
R_{20}^n	normalised 20-year return load
RAM	random array model
RAO	response amplitude operator
$R_{\max}$	short-term load
s	source wave energy converter
S	wave energy converter spacing
S_g	grid spacing (*GAM*)
S_{ij}	spacing between WEC i and j (*RAM*)
S_k	inter-device spacing of WECs for an array 'k' (*LAM*)
$S_{p,l}$	power spectral density of the l^{th} sea state
S_{rk}	spacing of rows (*LAM*)
t	target wave energy converter
t_s	sea-state duration
T_{hammer}	hammer blow period
T_{install}	installation duration (in days)
T_m	mean wave period
T_n	instantaneous tether vector ($n = 1,2,3$)
T_p	peak wave period
T_{pd}	driving duration (in seconds) for each pile
T_{pp}	preparation duration of each pile
$T_{p,wa}$	probability-weighted average wave period
$\widehat{\boldsymbol{U}}$	vector of complex velocity amplitudes
$\widehat{\boldsymbol{U}}_{\text{opt}}$	optimal complex velocity amplitudes
V	undirected weighted graph vertices
w	undirected weighted graph weights
w_{steel}	total weight of steel
WEC	wave energy converter
x_i, y_i	cartesian coordinates of WEC i
α_{ap}	tether's attachment point angle
α_{H}	tether's horizontal angle
α_i	contingency factor
α_f	pile fabrication factor
α_{v}	tether's vertical angle
α_x and α_y	grid coordinates (*GAM*)
β	wave direction
β_m	mean wave direction
β_{WA}	weighted average mean wave direction
γ	peak enhancement factor
γ_m	material factor
δ	angle between α_x and α_y (*GAM*)
δ_f	constant volume interface angle
ΔL_n	change in the tether length
$\Delta \dot{L}_n$	rate of change in tether length
θ_g	farm orientation (*GAM*)
θ_k	orientation of the array 'k' (*LAM*)
ϑ	decision variable
ξ_{heave}	heave amplitude
σ	standard deviation
σ_r^2	variance of the load
$\sigma_{\dot{\xi}_{\text{heave}}}$	standard deviation of the heave displacement
τ_f	local shaft friction
ω	angular frequency
*	complex conjugate transpose

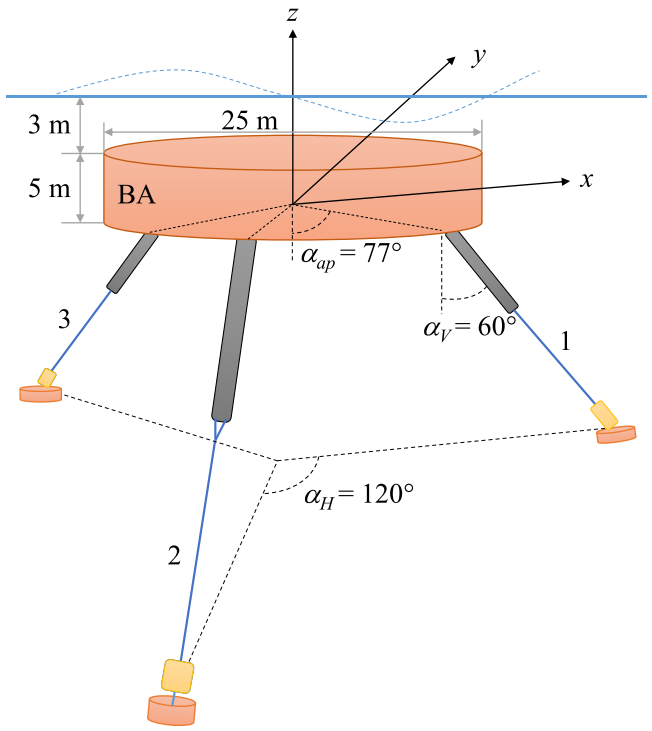

Fig. 1. Sketch of the shallowly submerged cylindrical point absorber with three taut tethers.

the practical design of WECs in realistic seas. Therefore, it is more practical to design array systems that can reduce destructive interactions (McIver, 1994; Weller et al., 2010).

Several studies have utilized different optimisation algorithms to identify the constructive interaction regimes in a wave farm to maximize power production (e.g., Child and Venugopal 2010, Giassi and Göteman 2018, Mercadé Ruiz et al. 2017, Neshat et al. 2020). Recently, Göteman et al. (2020) presented a comprehensive review of existing wave farm optimisation approaches that used different hydrodynamic modelling methods, power take-off (PTO) modelling and highlighted the associated challenges. This review indicated that a majority of existing studies have used only one objective, namely to maximise power generation. They also found that to maximise power production WECs in an array should generally align perpendicular to the wave direction, especially for long-crested waves.

One of the key challenges faced by the wave energy industry is cost competitiveness with other renewables. For energy projects, cost is generally quantified using the levelized cost of energy (LCoE), which is defined as the ratio between the total cost (including the capital, operational and maintenance costs) and the discounted present-day value of the energy produced throughout the operational life. While some studies have evaluated the LCoE of arrays after optimising for power production (e.g., Giassi et al. 2020, Sharp and DuPont 2018), optimisation should ideally concurrently consider power production and cost. This is due to the fact that some factors that maximise the power produced will increase cost, potentially more than offsetting the increase in power output. Therefore, it is important for WEC array developers to have tools to consider the array design in a multi-objective sense, using more comprehensive objective functions to aid in designing a wave farm. Existing studies have applied the multi-objective optimisation to many fields (e.g., Birk 2009, Fox et al. 2019, Karimi et al. 2017, Rodrigues et al. 2016) with only a few studies focussing on wave farms (Arbonès et al., 2018, 2016).

In this work, we develop a multi-objective optimisation framework that can be applied to optimise WEC arrays considering power output as well as a range of factors that impact cost. To demonstrate the methodology, a case study is conducted for Albany, Western Australia, with wave farms composed of several shallowly-submerged cylindrical WECs resembling Carnegie Clean Energy's CETO-6 device (Fig. 1). We consider some of the major cost components of wave energy projects, for example, foundations and cabling, using values from the available literature. However, the cost model for a particular wave energy project will vary with the WEC design and location (De Andres et al., 2017; Sergiienko et al., 2018), and thus our focus is primarily on demonstrating the multi-objective methodology that can subsequently be applied by wave energy developers using their own more complete, bespoke cost models.

This paper is organised as follows. Section 2 provides a detailed description of the method along with the objective functions and constraints used in the optimisation. In Section 3, we present the results for a few different array sizes. Some of the uncertainties associated with the optimisation are discussed in Section 4. Finally, we summarize our findings in Section 5.

2. Methodology

2.1. Wave energy converter

In this work, we consider a shallowly-submerged nearshore point absorber type WEC similar to Carnegie's CETO-6 device (Fig. 1). The geometric parameters of the WEC, including the diameter and height of the 'buoyant actuator' (BA) were kept constant throughout the study as 25 m and 5 m, respectively. The device was moored to the sea bed in 34 m of water and the BA submergence fixed at 3 m. The BA is moored using three taut tethers connected to distinct power take-offs (PTOs) capable of behaving as a spring-damper and allowing power generation from multiple modes of motion. Each tether's vertical (α_V) and horizontal (α_H) angles were fixed at 60° and 120°, respectively.

2.2. Multi-objective optimisation

Unlike single-objective optimisation, multi-objective optimisation deals with a set $\boldsymbol{f} = \{f_1, f_2, \ldots, f_n\}$ of n objective functions ($\boldsymbol{f}$) simultaneously, with the aim of finding a set of non-dominated (also called *Pareto* optimal) solutions subject to constraints. For more details on non-dominated solutions and sorting, readers are referred to Birk (2009) and Deb et al. (2000). The concept of multi-objective optimisation is not new, with several existing studies having applied the framework in different fields, including WEC geometries (Kurniawan and Moan, 2013), offshore structures (Birk, 2009), wind farms (Karimi et al., 2017; Rodrigues et al., 2016) and wave farms (Arbonès et al., 2018, 2016). The work on wave farms (Arbonès et al., 2018, 2016) had a focus on maximising power absorption, minimising the transmission cable lengths and minimising the wave farm area. The study demonstrated an increase in power absorption of roughly 1% (on average), with reduced transmission cables and farm area over the initial best-structured arrangement of WECs. Here we expand on the existing approaches by including different array layout models (Section 2.3) with a different evolution strategy of arrays (Section 2.8) and a larger set of objective functions including minimising foundation loads and the number of anchors (Section 2.7). Furthermore, by using a representative cost model we demonstrate the potential trade-offs between the converged wave farms.

Wave farm optimisation becomes increasingly complex as the number of objective functions and parameters increases. For a wave farm, the number of WECs in the farm, moorings or anchors (loads when shared or unshared), PTO capacity and control settings, electrical systems, transmission cables, sub-stations and grid connections could be considered. Omitting or approximating some of the important aspects of the farm might result in sub-optimal wave farm configurations. On the other hand, considering the full spectrum of variables involved in wave farm optimisation will increase the computational expense of any study (and complicate the interpretation of the output). To demonstrate the

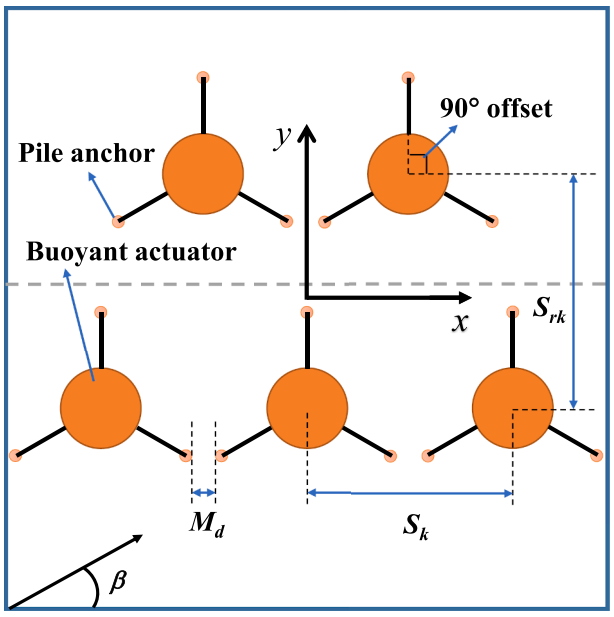

Fig. 2. Schematics of an example linear array setup for 5-WEC array arranged in 2 rows with orientation θ_k set as 0°. S_k is the inter-device spacing, S_{rk} is the row spacing, M_d is the distance between moorings and β is the wave direction. The grey dotted line indicates the major axis of the wave farm.

method, in this paper we choose to focus on a subset of the most important possible objective functions, but note that the method can accommodate additional parameters if sufficient computational resources are available.

The objective functions considered here are broadly fixed to maximise the power generation and minimise the capital cost. For the latter, we considered three variables (objective functions) that strongly influence the overall capital cost and vary with WEC farm configuration, specifically: the length of transmission cables, the number of foundations, and the design load for the foundations (which dictates their size). It is important to highlight here that we include in our optimisation costs that are likely to be dependant on WEC farm configurations rather than 'fixed costs' such as WEC manufacturing, contingencies and mobilisation. Although the costs associated with the BAs and PTOs account for a major proportion of the WEC farm cost, we assumed that each WEC in the array was of identical design and thus that the PTO costs are fixed (based on the best design).

In total, four objective functions are considered in this work with some conflicting with each other. For example, increasing the power generation typically increases the design load on the foundations and thereby cost. Also, to reduce the transmission cable lengths and to reduce the number of foundations (by using shared foundations), the WEC spacing must be reduced, which may impact the WEC-WEC interactions and alters the power generation in a nontrivial way. In such scenarios, multi-objective optimisation can provide a quantitative insight into the trade-off between multiple optimal solutions, in a way that a single-objective optimisation cannot. The benefits of multi-objective optimisation, as compared to single objective, have been demonstrated in different applications (e.g., Mahrach et al. 2020, Schulze-Riegert et al. 2007, Zakaria et al. 2012).

Our approach is based on the evolutionary multi-objective optimisation framework (also referred to as the MOEA approach, Deb 2011). The MOEA is a stochastic optimisation method and a population based computation similar to other evolutionary algorithms (e.g., Genetic Algorithm, Differential Evolution). In the MOEA and other evolutionary algorithms, the population size (*PopSize*) is one important component that can greatly influence the computational time and the converged solutions. Here, we refer to *PopSize* as the number of different arrays evaluated at each iteration. Reducing the *PopSize* may sometimes lead to sub-optimal solutions (Koumousis and Katsaras, 2006; Pelikan et al., 2000), conversely, increasing the *PopSize* could result in the algorithm expending more time finding the optimal solutions (Lobo and Goldberg, 2004; Roeva et al., 2013). There is a trade-off between computational time and the accuracy of the converged solutions. In this work, the *PopSize* is fixed as 75, based on our initial trials with 5- and 7-WEC farms and found to be efficient in terms of both computational time and convergence rate.

The optimisation procedure involves 5 broad steps: (i) initializing the wave farms (arrays), (ii) evaluating each objective function for each array, (iii) non-dominated sorting to identify the *Pareto* optimal solutions, (iv) generating new wave farms by variation of the non-dominated solutions and (v) repeating steps (ii) to (iv) until the specified stopping time.

2.3. Array models

The first step in the optimisation is to initialize arrays; here the number of arrays is dictated by *PopSize* (75). Existing studies have used different approaches to design arrays, ranging from structured arrangements of WECs (López-Ruiz et al., 2018; Mercadé Ruiz et al., 2017) to random placements (Neshat et al., 2020) and random gridded arrangements (Giassi and Göteman, 2018; Sharp and DuPont, 2018), with several early studies focussed on linear arrangements of WECs (e.g., Kagemoto and Yue 1986, Thomas and Evans 1981). A recent study showed that regular line arrays optimised for a given wave spectrum generally outperform the best random arrays of the same size for that spectrum (Tokić and Yue, 2021). However, it is still not clear how the different array approaches perform in the multi-objective space. Therefore, in this study, we used three different array layout models; the *linear array model* (*LAM*), the *random array model* (*RAM*) and the *grid array model* (*GAM*). Each array model has different default arrangements and is described briefly here.

In the *LAM,* we considered linear rows and arrays, and reduced the number of design variables associated with the layout of the array to four. For an array *k*, the variables are inter-device spacing of WECs (S_k), the orientation of the farm, defined by the angle the tangent to the rows makes with the *x*-axis (θ_k), number of rows (r_k) and spacing of rows (S_{rk}). The variables are subject to the following constraints (see also Fig. 2):

$$\begin{cases} 97\ m \le S_k \le 300\ m \\ 0^{\circ} \le \theta_k < 360^{\circ} \\ 50\ m \le S_{rk} \le 300\ m \\ r_k = 1, 2, 3\ rows \end{cases} \forall\ k = 1, 2, \ldots, PopSize. \quad (1)$$

In addition to the above constraint, we also ensured that layouts satisfied the following constraint,

$$S_{ij} = \sqrt{(x_i - x_j)^2 + (y_i - y_j)^2} \ge 97\ \text{m}, \quad (2)$$

where x_i, y_i are the Cartesian coordinates of WEC *i*.

The limits applied to inter-WEC spacing are: a minimum limit of 97 m, which is as the spacing suitable for adjacent WECs in the array to share foundations (based on a 60-degree angle of the mooring line to the WEC and a depth of 34 m), and a maximum limit of 300 m, based on practical considerations to limit the area occupied by the array. Although the minimum row spacing is fixed as 50 m, a wave farm layout with minimum inter-WEC spacing along a row (= 97 m) and minimum row spacing (= 50 m) is not feasible as it would violate the minimum distance between any two WECs in the array, Eq. (2). Nevertheless, the minimum row spacing of 50 m was found to be useful in reducing the transmission cable length for layouts with inter-WEC spacing above 125 m.

The tether orientation is another important parameter that can have a major influence on foundation sharing. For a three-tethered CETO-like design, it is possible to share foundations with suitable spacing and

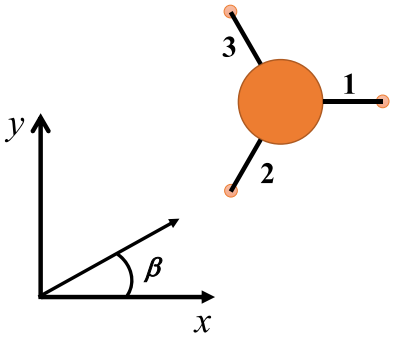

Fig. 3. Orientation of the tethers for WECs that are not sharing a foundation in the random array model (*RAM*). β is the wave direction.

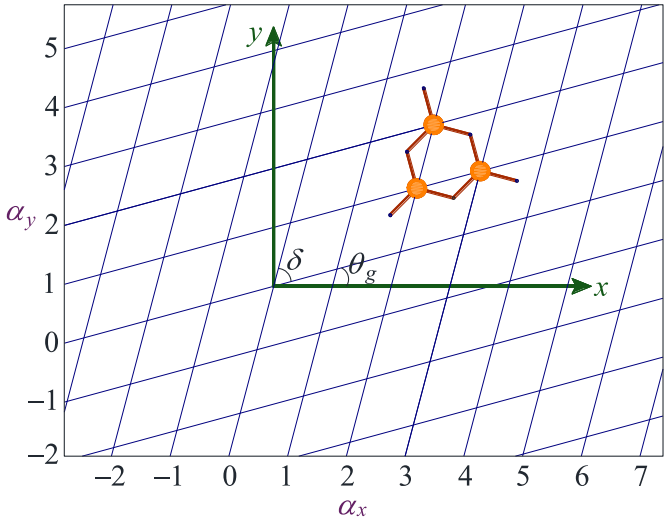

Fig. 4. Grid array description.

orientation. In the *LAM,* the tether orientation is fixed by the array orientation (θ_k). To effectively share foundations between WECs, a tether arrangement in which one tether points exactly normal to the row in the downwave direction is considered. Furthermore, for every array, we also calculated the distance between foundations (M_d). For arrays with $M_d \leq 3$ m, we modify S_k/S_{rk} such that WECs share anchors. Fig. 2 shows the schematics of the linear array arrangement for an illustrative array arranged in 2 rows with θ_k set to 0°.

As the positions of individual WECs in the *LAM* arrays are significantly constrained (i.e. S_k, θ_k and S_{rk} are constant), we consider the *random array model* (*RAM*) as our second array model. In the *RAM*, each WEC within the array is placed independently and subject to the constraint given in Eq. (2). In addition, for the *RAM,* we imposed a domain size limit, beyond which WECs cannot be placed. This constraint was expressed as,

$$\begin{cases} 0 \leq x_i \leq x_{\max} \\ 0 \leq y_i \leq y_{\max} \end{cases} \forall\, i = 1, 2, \ldots, \mathrm{N}, \tag{3}$$

where $x_{\max} = y_{\max}$ (square domain) and N is the total number of WECs in the array. Therefore, in the *RAM*, the array is described by 2 N variables.

In the *RAM*, the spacing S_{ij} is evaluated at each iteration and modified to facilitate sharing when $S_{ij} \leq 102$ m. This constraint is to maintain a minimum distance between the foundations and to increase the capability to share foundations in the *RAM.* Unlike the *LAM,* in the *RAM,* the tether orientation may be different for each WEC, depending on the arrangement necessary to enable foundation sharing. Due to the equiangular (in the horizontal plane) tether arrangement for the CETO-6 device, the mooring coordinates can be easily identified by knowing the coordinates of one mooring point (foundation sharing coordinate). Once all the three mooring points are fixed, the tether orientation of each WEC with respect to the x axis can be easily calculated. In the *RAM,* adjusting S_{ij} between two WECs may alter the inter-device spacing with other WECs in the array, which in turn may or may not further share foundations with the neighbouring WECs. Furthermore, S_{ij} adjustment may also re-orientate the tether arrangements of neighbouring WECs if additional WECs share foundations. Therefore, the modification (of S_{ij}) and re-orientation (of tether arrangement) are forced in a "repeat-until" loop with the stopping criteria set as "no change" in the Cartesian coordinates and mooring points of all WECs compared to the previous evaluation, or the maximum number of evaluations (10^5) being reached. The modified Cartesian coordinates are subjected to the spacing and domain size constraints, Eqs (2) and (3), inside the "repeat-until" loop. For WECs that are not sharing a foundation, the mooring arrangement is fixed with one tether pointing in the x direction and the other two tethers obliquely pointing in the opposite direction (see Fig. 3). Note that for the linear analysis used here to calculate the power production (see Section 2.3 below), the tether arrangement does not influence the absorbed power.

With the *LAM* and the *RAM*, foundation sharing of WECs is not always possible due to the spacing constraint for foundation sharing. Therefore, to consider foundation sharing effectively, we used the *grid array model* (*GAM*). In the *GAM*, the WECs are represented based on grid coordinates, α_x and α_y (Fig. 4).

The angle (δ) between α_x and α_y is fixed as 60° and grid points are spaced equally such that the WECs in adjacent grid points share at least one foundation. Furthermore, to include the wave farm orientation we introduced another variable referred to as the "farm orientation", θ_g, which applies to the entire array and not for individual WECs. Therefore, in the *GAM,* a wave farm is described by three variables: α_x, α_y and θ_g. Like the *LAM* and the *RAM,* the *GAM* is also subject to constraints as follows:

$$\begin{cases} -\alpha_{x,\max} \leq \alpha_{x,i} \leq \alpha_{x,\max} \\ -\alpha_{y,\max} \leq \alpha_{y,i} \leq \alpha_{y,\max} \end{cases} \forall\, i = 1, 2, \ldots, N, \qquad 0 \leq \theta_g \leq 2\pi \qquad \theta_g \in \mathbb{R}, \tag{4}$$

where $\alpha_{x,\max} = \alpha_{y,\max}$, and are fixed based on the number of WECs. The Cartesian coordinates are related to the corresponding grid coordinates as

$$\begin{bmatrix} x_i \\ y_i \end{bmatrix} = \begin{bmatrix} \cos\theta_g & -\sin\theta_g \\ \sin\theta_g & \cos\theta_g \end{bmatrix} \begin{bmatrix} \dfrac{\alpha_{y,i}}{2} - \alpha_{x,i} \\ \left(\alpha_{y,i}\right)\sqrt{3}/2 \end{bmatrix} S_g. \tag{5}$$

where S_g is the grid spacing (fixed as 97 m to allow foundation sharing for the chosen tether inclination and water depth).

Once the array is initialized using one of these methods, i.e. the *LAM,* the *RAM* or the *GAM,* we apply the optimisation procedure described in Fig. 5. The optimisation was carried out for each array model independently. The objective functions, viz. power generation, transmission cable length, number of foundations and loads, were subsequently evaluated. We describe the method employed to compute each of the objective function values in the next sections.

2.4. Array power

The total time-average power produced by an array of N WECs oscillating in six degrees of freedom, following linear wave theory, is calculated as (Budal, 1977; Falnes and Budal, 1982; Thomas and Evans, 1981)

$$P = \frac{1}{4}[\widehat{\boldsymbol{U}}^{*}\widehat{\boldsymbol{F}_e} + \widehat{\boldsymbol{F}_e}^{*}\widehat{\boldsymbol{U}}\,] - \frac{1}{2}[\widehat{\boldsymbol{U}}^{*}\boldsymbol{B}\widehat{\boldsymbol{U}}], \tag{6}$$

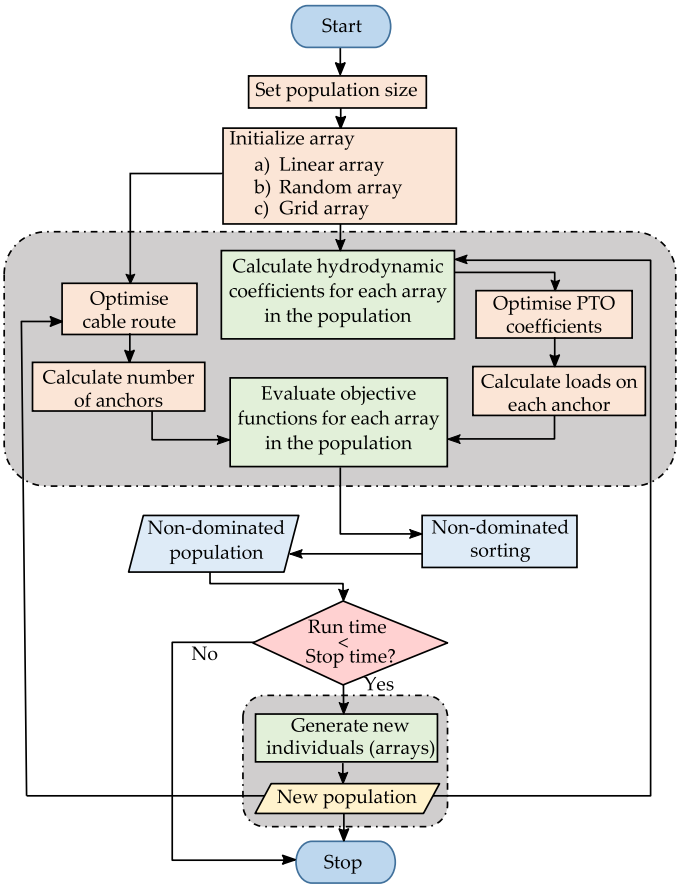

Fig. 5. Flow chart of the multi-objective optimisation.

where $\widehat{U}$ is the vector of complex velocity amplitudes, $\widehat{F_e}$ is the vector of complex excitation forces, $\boldsymbol{B}$ is the matrix of radiation damping coefficients and the asterisk in the superscript implies the complex conjugate transpose. $\widehat{U}$ is a frequency domain solution to the linear equation of motion given by (Falnes, 2002)

$$\widehat{F_e}(\omega) = \left[\mathrm{i}\omega(\boldsymbol{M}+\boldsymbol{A}_m) + \left(\boldsymbol{B}+\boldsymbol{B}_{\mathrm{pto}}\right) + \frac{\boldsymbol{K}_{\mathrm{pto}}}{\mathrm{i}\omega}\right]\widehat{U}(\omega), \tag{7}$$

where $\boldsymbol{A}_m(\omega)$ and $\boldsymbol{B}(\omega)$ are the frequency-dependant added mass and radiation damping matrices, $\boldsymbol{M}$ is the mass matrix, $\boldsymbol{K}_{\mathrm{pto}}$ and $\boldsymbol{B}_{\mathrm{pto}}$ are the linearized PTO spring and damping coefficient matrices. For the case of a three-tether WEC considered here, Orszaghova et al. (2020) developed solutions for Eq. (7) by assuming the PTO coefficients were identical for all three PTOs (refer to that study for further details). The hydrodynamic coefficients were obtained from a linear potential flow model (McCauley et al., 2018) which also accounts for array interactions. For the fully submerged device, the hydrostatic stiffness is zero and the restoring force is achieved mechanically through the PTO.

Apart from the placement of each WEC in the array, the PTO coefficients are another set of design variables to be optimised. In this study, for a given array, the PTO coefficients for each WEC may differ but are constant across all sea states, and are optimised to maximise the array power output. To optimise the PTO coefficients, we utilized the MATLAB (The Mathworks, Inc. MATLAB, Version 9.6, 2019) built-in global optimisation toolbox (Pattern Search algorithm). In order to validate the PTO coefficient optimisation, we first considered an array of 5 WECs with 3 oscillating modes (i.e. surge, sway and heave) and independent PTO settings for each mode, for which a theoretical optimal solution exists. The WECs were arranged in a single row (see Fig. 6a), exposed to long-crested regular waves. To include the influence of the sway mode, the WECs were exposed to waves at an angle of 45°. The maximum power ($P_{\max}$), given as,

$$P_{\max} = \frac{1}{8}\left[\widehat{F_e}^{*}\boldsymbol{B}^{-1}\widehat{F_e}\right], \tag{8}$$

occurs when

$$\widehat{U}_{\mathrm{opt}} = \frac{1}{2}\left[\boldsymbol{B}^{-1}\widehat{F_e}\right]. \tag{9}$$

Eq. (7) can then be rewritten as

$$\left[\boldsymbol{B}_{\mathrm{pto}} + \frac{\boldsymbol{K}_{\mathrm{pto}}}{\mathrm{i}\omega}\right]\widehat{U}_{\mathrm{opt}} = \widehat{F_e} - \left[\mathrm{i}\omega(\boldsymbol{M}+\boldsymbol{A}_m)+\boldsymbol{B}\right]\widehat{U}_{\mathrm{opt}} \tag{10}$$

by replacing $\widehat{U}$ with $\widehat{U}_{\mathbf{opt}}$ and by restricting B_{pto} and K_{pto} to be diagonal matrices. Solving each row independently, the theoretical optimal PTO coefficients for each individual WEC mode can be obtained. Fig. 5b–d show the validation of the PTO optimisation. The optimisation function locates the correct solution, providing confidence in the methodology. Depending on the initial guess, the optimisation took about 100 to 400 iterations and approximately 180 to 370 s of runtime on a quad-core desktop PC to find the theoretical optimum. For the theoretical validation, no constraints on the individual device PTO coefficients, namely stiffness (k_{pto}) and damping (b_{pto}) were imposed. However, in the remainder of the paper, for multi-objective optimisation, the coefficients were restricted to

$$\begin{cases} 5\times10^{5} \le k_{pto,i} \le 10^{7}\ \mathrm{N/m} \\ 10^{6} \le b_{pto,i} \le 10^{7}\ \mathrm{N/(m/s)} \end{cases} \forall i = 1, 2, \ldots, \mathrm{N}. \tag{11}$$

This imposed range of k_{pto} and b_{pto} was found to be sufficient, as the optimised coefficients were found to be well within the lower and upper

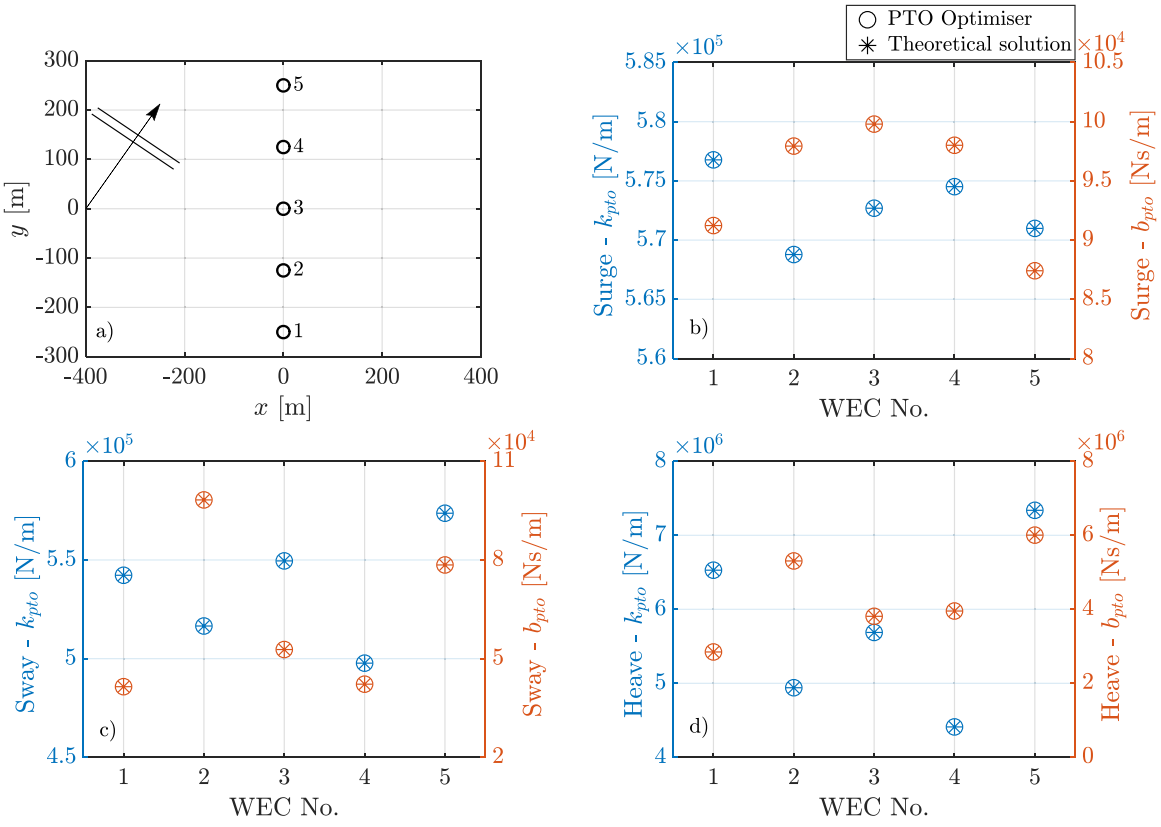

Fig. 6. Validation of PTO optimisation for 5 WECs in 3 modes (surge, sway and heave) arranged in a single row exposed to a regular wave of 1 m amplitude and 10 s period. The layout is shown in (a), the optimum damping coefficients and stiffness coefficients from both theoretical solution and PTO optimiser for surge, sway and heave modes are shown in panels (b), (c) and (d) respectively.

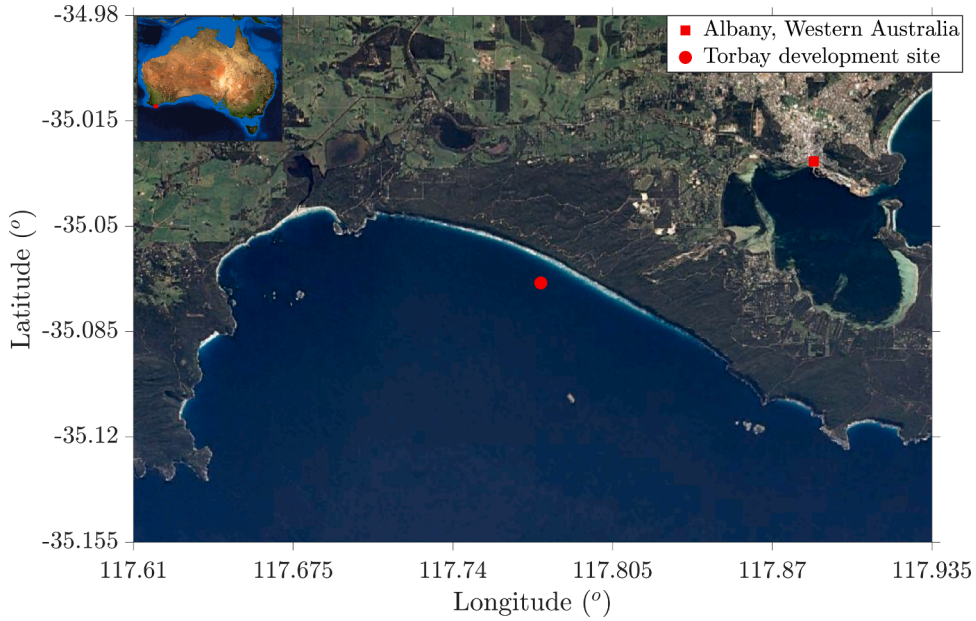

Fig. 7. Torbay in the Albany region of Western Australia. The inset image on the top left shows the map of Australia with the red square marking Albany. The red circle marks the Torbay wave energy development site and the location of the wave buoy.

bounds. For example, for the isolated WEC, the k_{pto} and b_{pto} were optimised as 4.2×10^6 N m^{-1} and 2.3×10^6 N m^{-1} s, respectively. Each WEC can move in all 6 degrees of freedom (surge, sway, heave, roll, pitch and yaw); however, in the linearized system, all modes apart from yaw contribute to power production (Orszaghova et al., 2020).

We used wave data from Torbay near Albany in Western Australia (Fig. 7) to define the input wave climate (Fig. 8). Being exposed to consistent swells from the Southern Ocean, the site is recognized as a promising site for wave energy development. For more details on the seasonal and interannual variability of the site's wave climate, refer to

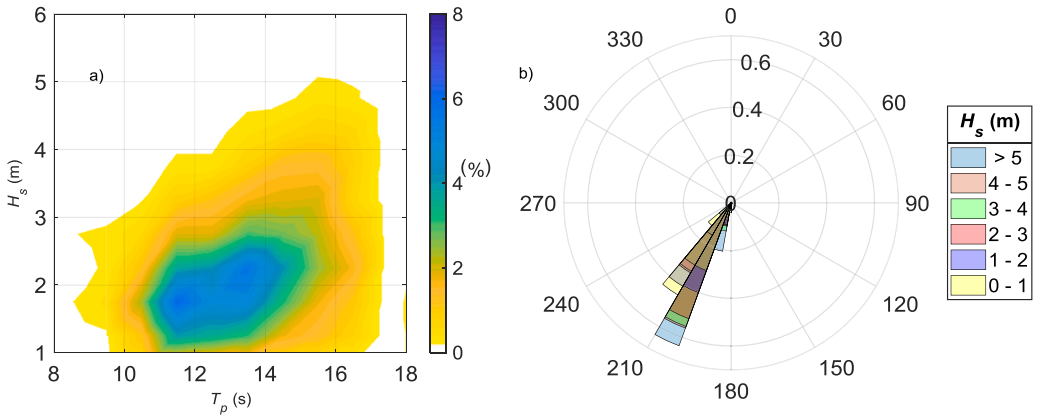

Fig. 8. Wave climate at Torbay, Albany site in Western Australia. The joint occurrence distributions of H_s and (a) T_p; (b) β_m (°).

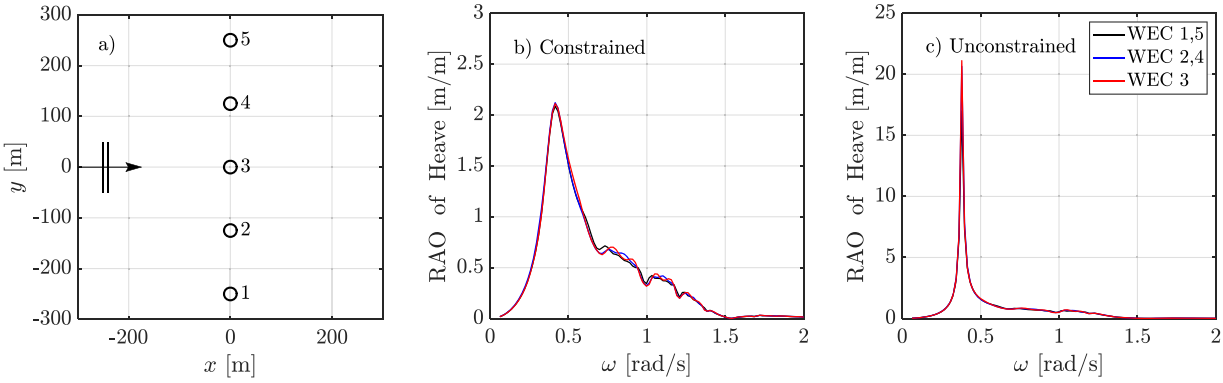

Fig. 9. Heave RAOs for 5-WECs arranged in a single row (a), when the PTO coefficients are optimised for a sea state with $H_s = 4$ m, $T_p = 15$ s, in constrained (b) and unconstrained (c) cases.

Cuttler et al. (2020). The Torbay wave climate (as derived from a directional wave buoy, see Fig. 8 and Cuttler et al. 2020) was used to calculate the mean power output as,

$$P_{\text{mean}} = \sum_{l=1}^{L} \left(P_l\left(H_s, \quad T_p, \quad \beta_m\right) O_l\left(H_s, T_p, \quad \beta_m\right)\right), \tag{12}$$

where H_s, T_p, and β_m are the significant wave height, peak wave period and mean wave direction. L represents the total number of sea states considered, O_l represents the probability of occurrence of the l^{th} sea state and P_l represents the power absorbed in the l^{th} sea state:

$$P_l = \int_0^{\infty} 2S_{p,l}\left(\beta_{m,l}, \omega\right) \frac{P\left(\beta_{m,l}, \omega\right)}{A^2} \mathrm{d}\omega, \tag{13}$$

where A is the incident wave amplitude and $S_{p,l}$ the power spectral density of the l^{th} sea state, here defined by a JONSWAP spectrum with peak enhancement factor $\gamma = 3.3$. In this work, we focused only on long-crested waves because the directional spreading at the Torbay site is rather low (mean directional spreading at the peak frequency of 17.5°); however, the methodology can be easily extended to study short-crested waves by integrating Eq. (13) over a range of wave directions, with $S_{p,l}$ being the directional spectrum. For more details on the incorporation of short-crested waves, readers are referred to Göteman et al. (2018).

2.5. Displacement constraint

In this work, the PTO is modelled as a linear spring-damper. Optimising the PTO coefficients to maximise the power absorption based on the frequency-domain solutions to the linear equation of motions may result in large displacement amplitudes of the WECs. Sometimes, the resulting displacement amplitudes can be unrealistic and, from a design and manufacturing point of view, very large displacements are costly to accommodate. In time-domain modelling, the displacements of each WEC (or the PTO stroke) can be limited using a hard-stop mechanism that exerts an additional force by adding a large spring stiffness coefficient (e.g., Babarit et al. 2012). In the frequency-domain modelling conducted here, we imposed this limit in a statistical sense. As the submergence depth is fixed at 3 m and the device generates much of its power from the heave motion, we imposed the following heave constraint:

$$\max\left(\left|\frac{\xi_{\text{heave}}}{A}\right|\right) \leq \frac{3 \times 2\sqrt{2}}{\max(H_s)}, \tag{14}$$

where $\max(H_s)$ is the largest H_s of all the sea states and $|\frac{\xi_{\text{heave}}}{A}|$ is the heave response amplitude operator (RAO). This constraint is derived by assuming that the standard deviation of the heave displacement is always less than $\max\left(|\frac{\xi_{\text{heave}}}{A}|\right) \frac{H_s}{4}$, since $\sigma^2_{\xi_{\text{heave}}} = \int_0^{\infty} |\frac{\xi_{\text{heave}}}{A}|^2 S_p(\omega)\mathrm{d}\omega$. Taking $3/\sqrt{2}$ m as the nominal limit of the standard deviation, we arrive at Eq. (14). This constraint does not guarantee that the instantaneous heave displacement will never be greater than 3 m, but it is simple and sufficient for our purpose, as we are interested not in individual events but in the effects of limiting the displacement on statistical quantities such as mean power output and most probable maximum loads, which we use in our objective functions.

As the displacement of each WEC depends on the PTO coefficients, we incorporated the displacement constraint inside the PTO

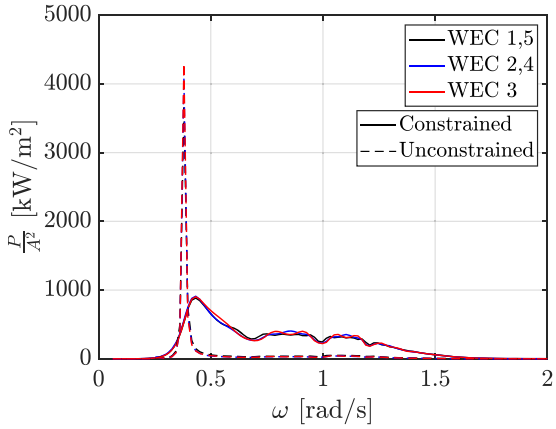

Fig. 10. Power absorption function of each WEC in the array corresponding to the constrained and unconstrained cases of Fig. 9 with $H_s = 4$ m, $T_p = 15$ s.

optimisation. Therefore, during the PTO optimisation, the optimiser searches for the PTO combinations that generate the maximum power given the displacement constraint in Eq. (14). In order to test the displacement constraint used in this work, we considered the same wave farm shown in Fig. 6a and subjected it to $H_s = 4$ m and $T_p = 15$ s. The heave RAOs with PTO coefficients optimised under constrained and unconstrained conditions are compared in Fig. 9b and c, respectively.

The mean (across the 5 WECs) standard deviation of the heave motion is about 0.61 m for the constrained case, whereas for the unconstrained case it is about 1.83 m. To quantify the difference in power absorption between the constrained and unconstrained cases, we compared the power absorption from the two cases in Fig. 10 for the same wave farm and PTO coefficients optimised under the same wave condition described in Fig. 9. In the unconstrained case, the mean absorbed power for $H_s = 4$ m and $T_p = 15$ s is about 770 kW, reducing to 530 kW (≈ 25% reduction) for the constrained case. This is expected and similar to existing studies, (e.g., Falnes and Budal 1982, Thomas and Evans 1981), that showed constraining the WEC motion resulted in reduced power absorption.

2.6. Load calculation

In a wave farm, moorings and foundations represent a significant proportion of the total capital cost of the project, (e.g., Neary et al. 2014). The foundation design must be adequate to withstand structural loading from extreme events. For the CETO-6 device, we considered a 20-year return load (R_{20}) as the design load for the pile anchor foundation. To estimate R_{20} we used linear wave-structure interaction theory and an approach given in Faltinsen (1990). Note that we are interested in how R_{20} changes as the array changes – we do not expect linear theory to give accurate predictions of extreme loads, but expect that it will give an indication of these changes. To calculate the load on each foundation, we first calculated the dynamic vertical load transfer function, $F_{l,n}$ ($n = 1,2,3$), considering linear spring and damping force, as

$$F_{l,n} = \left(k_{pto}\Delta L_n + b_{pto}\Delta \dot{L}_n\right)\frac{T_n}{|T_n|}.\widehat{k}, \tag{15}$$

where T_n is the instantaneous n-th tether vector from the attachment point to the seabed and $\widehat{k}$ is the unit vector in the vertical direction. Here ΔL_n and $\Delta \dot{L}_n$ are the change in tether length and the rate of change in tether length, both of which are a function of the displacements of the body (Orszaghova et al., 2020). Once F_l is obtained, the variance of the load σ_r^2 for different sea states are calculated from

$$\sigma_r^2 = \int_0^\infty S_p(\omega)\left|\frac{F_l}{A}(\omega)\right|^2 \mathrm{d}\omega. \tag{16}$$

We assume that the load amplitudes follow a Rayleigh distribution (like the wave amplitudes). With the joint probability distribution of significant wave height, peak wave period, and mean wave direction, the long-term probability that the peak value of the load does not exceed R is given in Faltinsen (1990) as

$$P(R) = 1 - \sum_{i=1}^{I}\sum_{j=1}^{J}\sum_{k=1}^{K} exp\left(-\frac{0.5R^2}{\left(\sigma_r^{ijk}\right)^2}\right)p_{ijk}, \tag{17}$$

where σ_r^{ijk} is the standard deviation of the load for the sea state defined by significant wave height index i, peak wave period index j, and mean wave direction index k, and p_{ijk} is the probability of occurrence for the sea state.

To estimate R_{20}, the number of cycles, N_c (for 20 years), is calculated from the probability-weighted average wave period ($T_{p,wa}$), i.e. $N_c = \frac{20\times365\times24\times3600}{T_{p,wa}}$. The probability level Q (= 1-$P(R)$) and the number of cycles N_c are related as $Q = 1/N_c$. Once Q is obtained based on N_c, the most probable maximum load R for the given probability level Q can be obtained from Eq. (17). The static pretension force, which is a function only of net buoyancy, is then added.

2.7. Objective functions

Maximising power generation was the first objective considered in this study. For convenience, we framed optimisation as the minimisation of objective functions. We used the interaction factor, also called the 'q' factor (Budal, 1977), which is the ratio of the power absorbed by the array to N times that produced by an isolated WEC (P_{iso}):

$$q = \frac{P_{\text{mean}}}{NP_{\text{iso}}}. \tag{18}$$

As we focused on minimising the objective functions, we used $1/q$ as the first objective function.

Minimising the export cable length (L_c) connecting all WECs in the farm to a sub-station was the second objective. For this, we utilized *Prim's* algorithm (Prim, 1957). Given the undirected weighted graph (V, E, w), where V, E, w are the vertices, edges and weights (distance) connecting the source s and target t WECs, the length of cable is:

$$L_c = \min \sum_{st\in E} w_{st}. \tag{19}$$

We normalised L_c by N times the minimum spacing (S) and used it as the second objective function.

Minimising the number of anchors in the wave farm (to reduce the capital and installation cost) was the third objective considered in this work. We first calculated the number of anchors (N_a) in the wave farm based on shared and unshared conditions and normalised it by N times the number of isolated WEC anchors:

$$N_a^n = \frac{(N_a)_{farm}}{3N}, \tag{20}$$

where N_a^n is the normalised number of anchors.

The fourth and final objective was to minimise the design load of the anchors. For the CETO-6 device, the R_{20} estimate for each foundation can be slightly different as it is supported by 3 taut tethers, the loads in which depend on the orientation of the tethers with respect to the incoming wave directions. In practice, the maximum R_{20} (amongst the three anchors) is used as the design load and applied for all three anchors. For the final objective function, we used the normalised load, R_{20}^n, which is the ratio of maximum R_{20} estimated for the farm to the

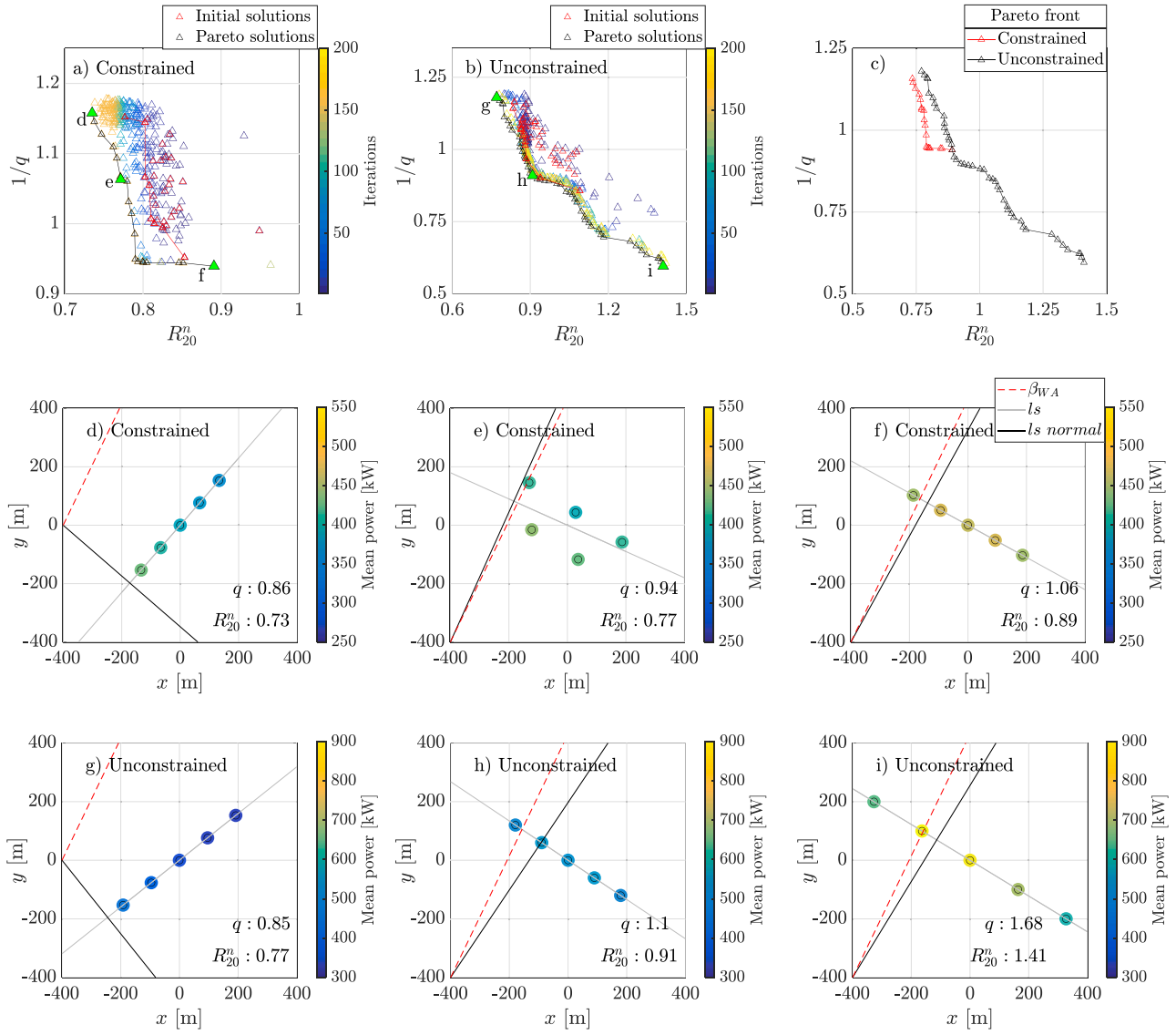

Fig. 11. Wave farm optimisation for 5-WECs under constrained (panel a) and unconstrained (panel b) cases considering 2 objectives (maximising power and minimising load) using the *LAM*. Pareto fronts from both cases are compared in panel c). The solutions highlighted (green triangles) in panel (a) and (b) are shown in panels (d)–(i).

maximum R_{20} of an isolated WEC with specific tether orientation that does not vary with iteration:

$$R^n_{20} = \frac{\max\left(R_{20,farm}\right)}{\max\left(R_{20,iso}\right)}. \tag{21}$$

Note that, for the shared foundation case, we sum the loads from the corresponding tethers which share a foundation. As the load transfer function is complex, the in-phase and out-of-phase loads are directly accounted for in the current methodology.

2.8. Evolution of arrays

Once the objective functions were evaluated for the wave farms generated in the first iteration, the solutions were subjected to a non-dominated sorting to identify the *Pareto* fronts, which were then used to generate the new offspring arrays. The evolutionary strategy to generate new offspring arrays is a crucial part of the optimisation as it influences the convergence rate of the optimal solutions. A recent study (Neshat et al., 2020) presents a comprehensive comparison of different evolutionary strategies and convergence rates of the optimal solution for a single-objective optimisation. In this study, we used a probability-based evolutionary strategy. The new array parameters in the offspring are generated based on a combination of normal and uniform distributions. In the random array model (*RAM*), the offset distance of WEC_i from its previous location is obtained from a normal distribution with mean 0 and standard deviation (σ), which varies with each iteration as

$$\sigma = \frac{1}{J^c} r_{\max}, \tag{22}$$

where J is the iteration number, $r_{\max}$ is a pre-selected radius of 250 m and c is a mutation coefficient chosen as 0.7. Further, the direction of the offset (0° to 360°) is obtained from a uniform distribution. Eq. (22) in combination with the non-dominated sorting is a simple but effective adaptive, robust approach that ensures quicker convergence of the *Pareto* solutions. Similar to the *RAM*, in the linear array model (*LAM*), the inter-device spacing S_k and row spacing Sr_k are obtained from a normal distribution with mean 0 and σ which changes with each iteration. Here the mutation coefficient c is fixed as 0.2, S_k and Sr_k are subject to the constraints given in Eq. (1). Further, θ_k is obtained from a continuous uniform distribution, whereas r_k is obtained from a discrete uniform distribution subject to the constraint in Eq. (1). Finally, for the

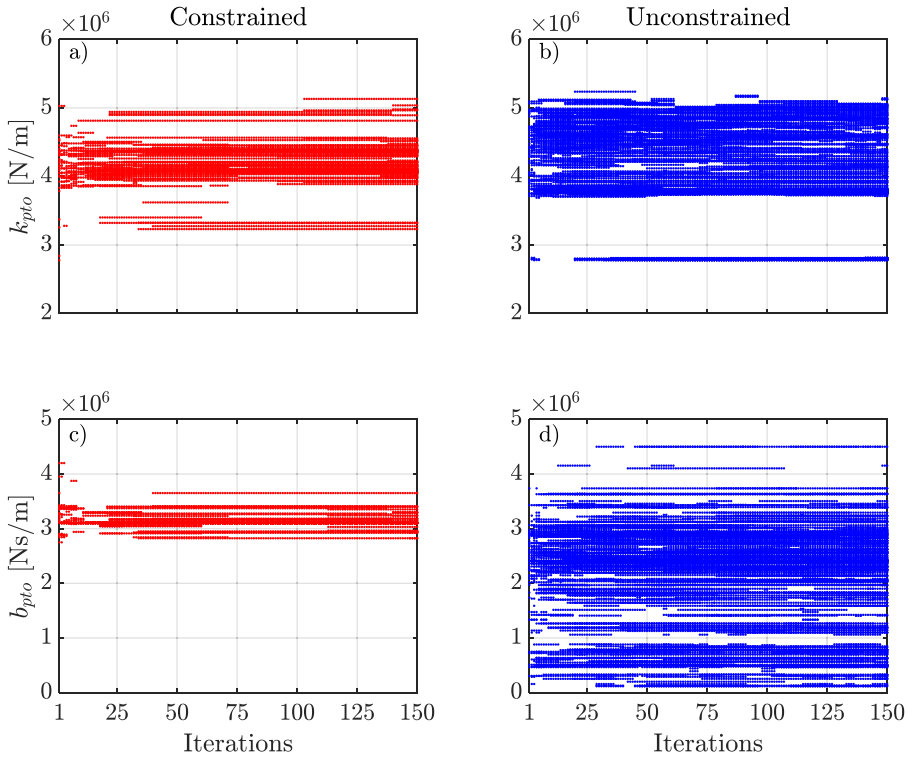

Fig. 12. Optimised PTO coefficients in the Pareto optimal solutions at different iterations for 5-WEC array in constrained and unconstrained cases with the *LAM*. Panel (a) and (b) correspond to the stiffness coefficients, k_{pto} N/m and panel (c) and (d) correspond to damping coefficients b_{pto} Ns/m.

grid array model (*GAM*), the grid coordinates α_x and α_y are obtained from a normal distribution with mean 0 and σ based on Eq. (22), but rounded to the nearest integer to align with the grid (see the grid axis in Fig. 3). For the *GAM*, the $r_{\max}$ is fixed as 4 for 5-WEC farm optimisation ($r_{\max} = 5$ and 6 for 10 and 20 WECs, respectively). The mutation coefficient c is fixed as 0.4 and kept the same for different numbers of WECs. Similar to the *RAM* and the *LAM*, the orientation of the farm (θ_g) is obtained from a continuous uniform distribution subject to the constraint in Eq. (4). The choice of parameters (c, r_{max}) for different array approaches were based on a number of trials with 5-WEC optimisations and found to influence the rate of convergence.

During our initial trials, some solutions in the *Pareto* front were close to each other and clustered at the objective space. Furthermore, during the non-dominated sorting of solutions (after the first iteration), the number of non-dominated solutions sometimes exceeded *PopSize*. This is due to the non-dominated sorting of the combined parent and offspring solutions. When the number of non-dominated solutions exceeds *PopSize*, only a limited subset of solutions (= *PopSize*) is transferred to the next iteration. To ensure that the solutions are well spread without discarding useful solutions and to avoid clustering of solutions, we used a clustering algorithm (Kurniawan and Ma, 2009). The clustering algorithm becomes active only when the number of non-dominated solutions is at least 80% of the *PopSize* or greater. The clustering algorithm first clusters the solutions based on the number of clusters assigned. For a *PopSize* of 75, the number of clusters was fixed as 60. The next step involves calculating the distance (d_c) between each cluster (e.g., C_i, C_j) in the objective space based on

$$d_{c(i,j)} = \frac{1}{|C_i||C_j|} \sum_{i \in C_i, j \in C_j} \sqrt{\sum_{k=1}^{n} \left(\frac{f_k(\vartheta^i) - f_k(\vartheta^j)}{f_k^{\max}(\vartheta) - f_k^{\min}(\vartheta)} \right)^2}, \tag{23}$$

where ϑ^i denotes the decision variable and $f_k(\vartheta^i)$ denotes the map of the decision variable in the objective space. The $|\ldots|$ implies the size of the clusters. The superscripts max and min denote the maximum and minimum function values, respectively.

If the number of clusters formed is greater than the number of clusters assigned, the clusters with minimum $d_{c(i,j)}$ are combined to form one cluster until the number of clusters equals the number assigned. The next step is calculating the centroid (e) of each cluster:

$$e_i = \frac{1}{|C_i|} \sum_{j \in C_i} (f_1(\vartheta^j), \ldots, f_n(\vartheta^j)). \tag{24}$$

Solutions with a minimum distance to each centroid are retained and the rest of the solutions are discarded. Once the required number of solutions (arrays) are obtained, new offspring (arrays) are generated. The new individuals are further evaluated, and the optimisation procedure described in Fig. 5 is repeated until the assigned stop time. In our optimisation runs, due to the clock limit in the computing resources, we fixed a stop time rather than specifying the number of iterations as the stopping criterion. The stop time (varying with the number of WECs) was fixed based on multiple runs and by analysing the final *Pareto* front being stable for at least the last 20 iterations.

3. Results

3.1. Constrained vs unconstrained body motion

To understand the influence of our displacement constraint on both power absorption and load (R_{20}), optimisation runs were carried out with the *LAM* for 5 WECs using two objective functions (power and load) (Fig. 11). To highlight the range of PTO coefficients given by the optimiser in constrained and unconstrained cases, we fixed the stiffness coefficient range to that shown in Eq. (11), whereas the damping coefficient range was fixed to between 1×10^5 and 1×10^7 Ns/m. Furthermore, to understand the significance of array interactions in both cases, we first calculated the ratio of the mean powers absorbed by an isolated WEC in constrained (P_{cons}) and unconstrained (P_{uncons}) cases. As a result of optimising PTO coefficients that are constant for all sea-states, the ratio of $P_{\text{cons}}/P_{\text{uncons}}$ was found to be 0.99. This is possible as the mean power absorption calculation also involves the probability of occurrence

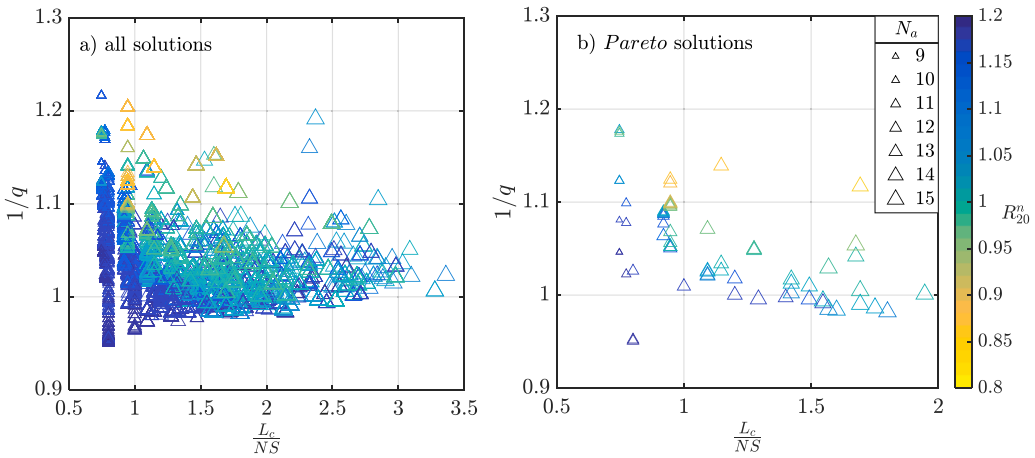

Fig. 13. Multi-objective optimisation for 5-WECs using the *GAM*. The axes represent 2 objective functions i.e. x – normalised cable length, y – inverted q factor. The marker size represents the third objective function, the number of foundations in the array (see scale in b) and the colours represent the fourth objective function, normalised load. The final *Pareto* solutions are shown in panel (b).

of each sea state (see Section 2.3). Similar to power absorption, the ratio of maximum R_{20} for an isolated WEC under constrained and unconstrained cases, $\max(R_{20,\text{cons}})/\max(R_{20,\text{uncons}})$, was found to be 0.95.

As we fixed both objective functions to work towards minimisation, the convergence of the *Pareto* front from the initial solutions (red triangles) to the optimal front (black triangles) can be distinguished using the colours representing the number of iterations (Fig. 11a, b). Although we achieved the optimal *Pareto* front in about 10–20 iterations (based on multiple trials), the optimisation was further extended to about 200 iterations to provide a further check on convergence. The *Pareto* fronts from the constrained and unconstrained cases are compared in Fig. 11c). Unlike the isolated WEC case, the difference between constrained and unconstrained cases in arrays is substantial. The constrained *Pareto* front resulted in reduced power absorption and also reduced R_{20} compared to the unconstrained front (Fig. 11c). This indicates the relative importance of array interactions under constrained and unconstrained cases.

As it is not feasible to show the array layouts of all the candidates in the *Pareto* optimal fronts, we show the farms favouring each objective function and one farm close to favouring both functions, (Fig. 11d–f) for the constrained case and (Fig. 11g–i) for the unconstrained case. To understand the influence of wave direction on the converged solutions, we plot the least square (*ls*) axis of the wave farms, the line normal to the *ls* axis (*ls normal*) and the weighted average wave angle (β_{WA}), which is based on the probability of occurrence at Torbay (Fig. 8b).

As might be anticipated, the farms generating maximum power mostly formed a single line with the *ls* axis close to perpendicular to the predominant wave direction. Farms with minimum load also formed a single row, but the *ls* axis was close to parallel to the predominant wave direction (Fig. 11d, g). Despite imposing the displacement constraint, we found a striking resemblance in some wave farms between the constrained and unconstrained cases e.g., Fig. 11f, h and 11d, g. Both farms were comparable in power generation and estimated maximum load. Another interesting result is the converged spacing S of 169 m for the maximum power generating wave farm in the unconstrained case is reduced to about 124 m in the constrained case. Despite having a larger domain and a significant range for spacing S between WECs, the average S in the *Pareto* optimal solutions in the constrained case ranged between 100 and 130 m (based on multiple trials). Constraining the WEC motion slightly modifies the power curve towards the higher frequency region (Fig. 10). This influences the distance for optimum WEC-WEC interaction, which in turn is reflected in the converged spacing.

In our study, the PTO stiffness and damping coefficients were optimised for the entire wave climate rather than for each sea state. In practice, the PTO coefficients can be optimised for each sea state or for a shorter duration. This indeed increased the mean power output, for which a considerable difference was observed between the varying PTO and uniform PTO cases, but the difference in terms of the 'q' factor was small (figure not shown). In both the unconstrained and constrained cases, PTO coefficients play a significant role in determining the power generation as well as the load R_{20}. To check the differences in the optimised PTO coefficients in both cases, we extracted the optimised coefficients for all wave farms in the non-dominated front at each iteration (Fig. 12).

For the isolated WEC, in the constrained scenario, the stiffness coefficient increased to about 1.07 times the unconstrained case, and the damping coefficient to 1.35 times the unconstrained case (Fig. 12). For the wave farms (with the *LAM*), the stiffness coefficient follows this trend with a small difference between constrained and unconstrained cases. The standard deviation was smaller for the constrained case compared to the unconstrained case. The damping coefficients were found to be widely spread for the unconstrained case, whereas the range was smaller in the constrained case (Fig. 12c, d). This is a result of the damping coefficients restricting the motion of WECs and the power generation which in turn also influences the R_{20}. As having constrained motions is more realistic for WEC deployments we focus on the constrained motions in the remainder of the paper.

3.2. Multi-objective optimisation – an illustrative example

The benefit of multi-objective optimisation is that we obtain a set of optimal trade-off solutions without requiring *a priori* knowledge of the relative importance of the objectives. From this set of optimal solutions, we can learn about the trade-off behaviour of the solutions on the *Pareto* front. In this study, we choose to explore the design space of nearshore submerged wave farms using four objective functions (Section 2.6) that are important in designing a wave farm. We consider three different array models (*LAM, RAM* and *GAM*) and carry out the optimisation runs independently; however, in this section, the result pertaining to 5-WEC optimisation using the *GAM* is discussed first. As the optimisation involves four equally weighted objective functions, the solutions are plotted with varying marker sizes (number of anchors) and colours (R^n_{20}) to differentiate in the objective space (Fig. 13).

From Fig. 13, we can learn about the trade-off behaviour of the optimal solutions. As the power absorption increases, the corresponding maximum load also increases (darker colours occur lower down on the plot). As the inter-WEC spacing decreases, the WECs move closer towards the anchor sharing grid points. This can be seen by the decrease in the number of anchors occurring with a decrease in the inter-WEC spacings (smaller markers at the left of the plot). Due to the presence of multiple objective functions (>2) in Fig. 13a, the convergence of

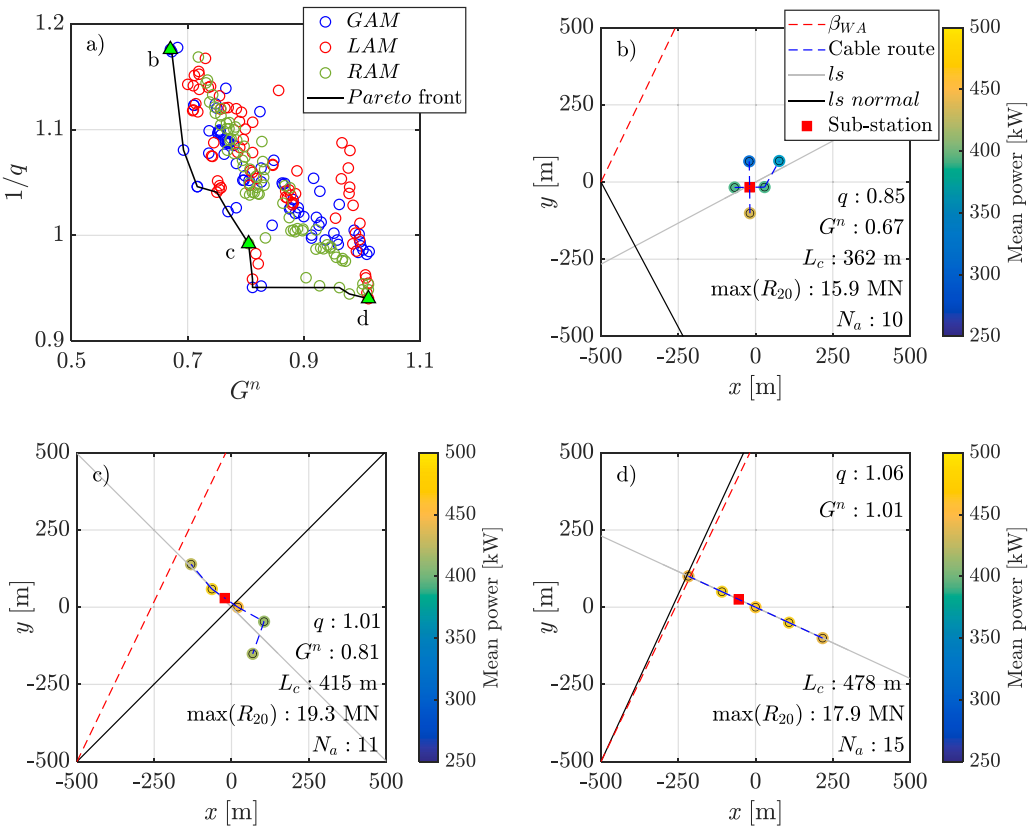

Fig. 14. Multi-objective optimisation for 5-WECs using three array models. Panel a) shows the post-processed solutions obtained from different array models and the *Pareto* front sorted by combining all solutions. The highlighted green triangles in the *Pareto* front are presented in panel b, c, d respectively, with colorbar indicating the mean power absorption and the black circle representing the WEC diameter (25 m).

Pareto solutions is more difficult to visualise than in the 2 objective optimisation e.g., Fig. 11a, b. Therefore, the final non-dominated *Pareto* solutions are shown in Fig. 13b separately. From this figure, we see that it is possible to get high power absorption with small inter-WEC spacing (and shared foundations), but not without increasing the loads. We also see that it is possible to reduce inter-WEC spacing without increasing the loads, but only up to a certain spacing, below which the loads increase. The number of anchors, on the other hand, do not have any effects on the absorbed power. Fig. 13 also shows, at least approximately, the minimum limits to the objective function values possible for the given problem, e.g., the minimum number of anchors possible for a 5-WEC array is 9. When the maximum power and minimum cable length is of interest, some of the converged solutions here are close to the converged layouts reached in existing studies (Arbonès et al., 2018; Giassi et al., 2020).

Once we identify the set of optimal solutions, the next step is to choose amongst these based on higher level information on the relative importance of the objectives. As a possible intermediate step, the design load, transmission cable length and number of anchors can be combined into a cost metric G, since they are related to the capital and installation costs. For this purpose, we utilized a method and cost parameters given by Gaudin et al. (2021). Noting that our primary focus is to demonstrate the methodology, we do not attempt to account for all costs or complexity in the cost model. For simplicity, only the cost factors associated with the objective functions are considered and the factors related to fixed costs (those that will not change based on array layout, including the BA and PTO in our example) are not considered. The design of the foundation pile is one critical step to calculate the cost of pile (both manufacturing and installation). We used the UWA-05 method (Lehane et al., 2007) to design the pile; for that, the cone tip resistance profile for a representative seabed condition was adopted from Cai et al. (2021), which is based on random field theory. Finally, by applying linear regression for a range of loads and the estimated cost, we arrived at Eq. (25) (see Appendix A for more details). The three objective function values (dimensional) from the multi-objective (four) optimisation runs are used to calculate G as,

$$G = \sum_{i}^{N_a}\left(\left(5.65\times10^{4}\right)R_{20,i} + 2.9\times10^{5}\right) + \left(0.4\times10^{3}\right)L_c + 4.5\times10^{6}, \quad (25)$$

where N_a represents the total number of anchors ($i = 1,2,\ldots, N_a$). For an isolated WEC, N_a and L_c are 3 and 0. The total cost of the farm is then normalised with N times the isolated WEC cost which we call G^n.

As we conducted the optimisation runs with different array models (*LAM, RAM* and *GAM*) independently, the *Pareto* front from each array model is extracted to calculate G. However, for comparison, the solutions are plotted together in Fig. 14.

Fig. 14 shows the post-processed *Pareto* solutions obtained from the three array models. By post-processing we mean collapsing the three cost-related objective function values into one, by applying the cost model in Eq. (25). As the wave farm layouts favouring power and cost were of primary interest, non-dominated sorting was performed for all the post-processed solutions to get the combined *Pareto* front from the three array models (Fig. 14a). Solutions from each of the three array models were present in the *Pareto* front. For illustrative purposes, three representative layouts are shown in Fig. 14b–d. The wave farm generating maximum power (Fig. 14d) formed a single row of WECs close to normal to the incident wave direction (β_{WA}). In contrast, the minimum G^n layout (Fig. 14b) formed 2 rows of WECs with a reduced number of anchors and reduced inter-WEC spacings. The farm close to favouring both objective functions (14c) formed nearly a single row of WECs with fewer anchors than Fig. 14d. As a result of anchor sharing, the maximum R_{20} increased compared to R_{20} without sharing (Fig. 14c, d). Furthermore, although the array shown in Fig. 14b shares multiple anchors, due

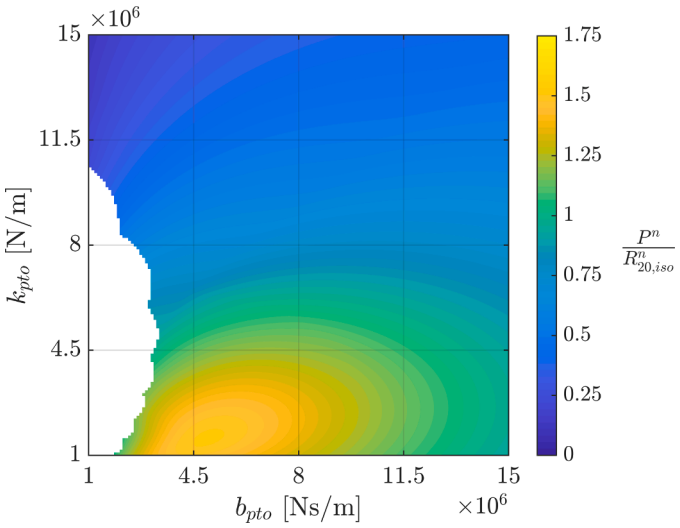

Fig. 15. The ratio of normalised power (P^n) over the normalised R_{20} ($R^n_{20,iso}$) for a range of PTO coefficients.

to the arrangement of WECs and cancellation of out-of-phase loads, the maximum R_{20} is less than the arrays shown in Fig. 14c, d. amongst the *Pareto* front solutions, the variation of q is relatively small compared to the variations of G^n.

It is worth mentioning that the sub-station was fixed close to the centroid of the wave farm with at least 50 m separation from any WEC in the farm as an additional constraint to avoid any intersections. Furthermore, the sub-station does not influence the array hydrodynamics and thereby power absorption or the loads.

The PTO coefficients play an important role in the conflicting objective functions as they impact power absorption and R_{20}. To explore potential trade-offs between power generation and R_{20}, we calculated the power generation and R_{20} for a range of PTO coefficients. We normalised the power obtained from a range of coefficients with the maximum power and call this normalised power P^n. Similarly, we normalised the R_{20} calculated for a range of PTO coefficients with the R_{20} estimated for the maximum power. We call this normalised load $R^n_{20,iso}$. Finally, we calculated the ratio of P^n over $R^n_{20,iso}$ for a range of PTO coefficients, as shown in Fig. 15 (a ratio greater than 1 is beneficial).

The PTO coefficient combinations violating the statistical displacement constraint are shown in white. Fig. 15 is calculated for a single WEC, but we expect similar trade-offs for WECs in a wave farm. Therefore, we completed additional optimisations where, in addition to searching for PTO coefficients that generate maximum power, we broadened the search space by calculating the power and loads for 9 additional unique combinations of PTO coefficients (which are picked randomly but within the range shown in Eq. (11)). Therefore, for a single wave farm layout, 10 different solutions are generated. As a result, for the total *PopSize* of 75 unique wave farm layouts, 750 solutions are generated. The solutions are further sorted using non-dominated sorting. The optimisation procedure described in Fig. 5 is applied and repeated until the assigned stop time.

Fig. 16 shows the post-processed *Pareto* solutions obtained from the three array models using PTO optimised to maximise mean power and random PTO search to explore the trade-offs. The structure of Fig. 16a is necessarily very similar to Fig. 14a when the power is close to maximum, but Fig. 16a has a significantly larger range of solutions with lower cost (and lower power). On comparing the solutions from three array models (Fig. 16a), the *GAM* appears to be dominating in the low-cost area of the *Pareto* front. In the *GAM*, the WECs in the neighbouring grids always share at least one anchor and this reduces the total number of anchors. As a result of the subsequent (random) PTO search, the load was also reduced and thereby the G^n, compared to Fig. 14a.

To address the effects of randomness in the optimisation at each

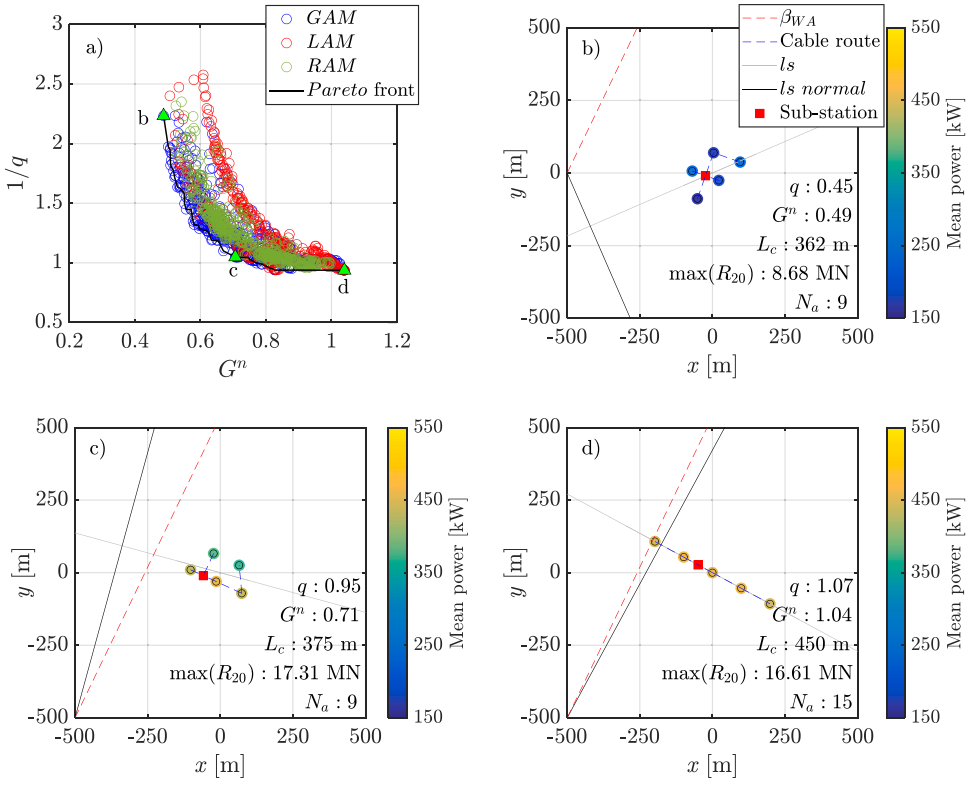

Fig. 16. Multi-objective optimisation for 5-WECs using three array models with PTO optimised to maximise mean power and random PTO search. Panel a) shows the post-processed solutions obtained from different array models and the Pareto front sorted by combining all solutions. The highlighted green triangles in the Pareto front are presented in panel b, c, d respectively, with colorbar indicating the mean power absorption and the black circle representing the WEC diameter (25 m).

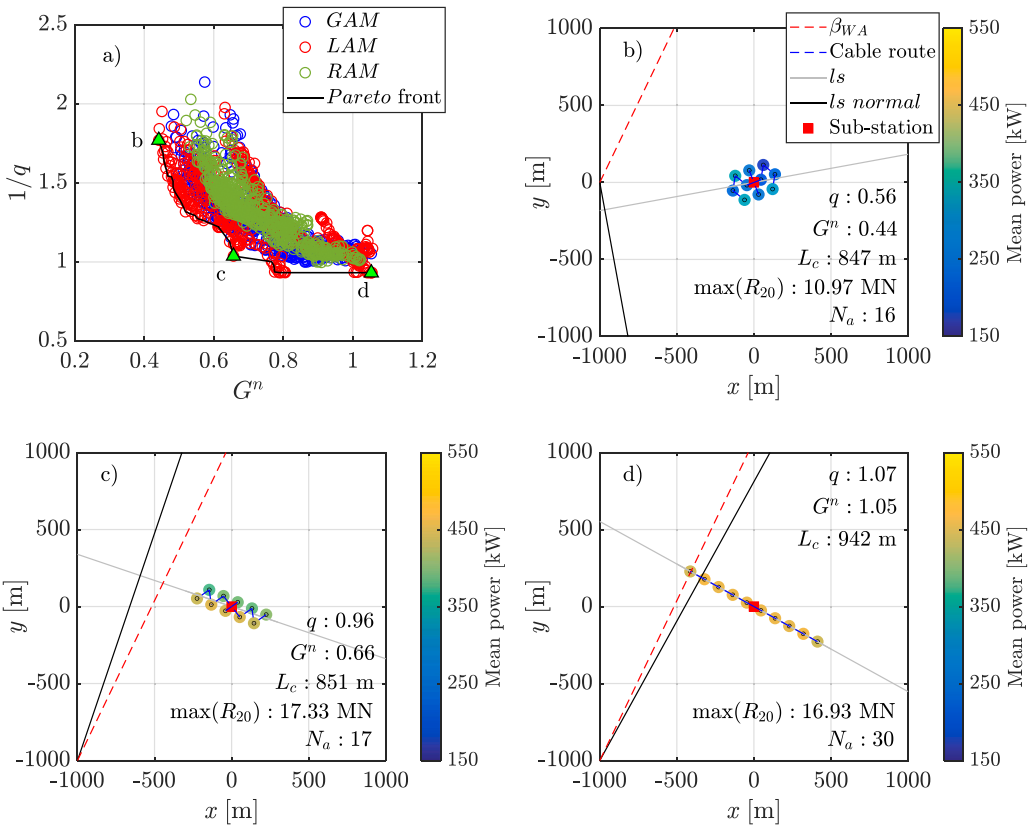

Fig. 17. As in Fig. 16 for 10-WECs.

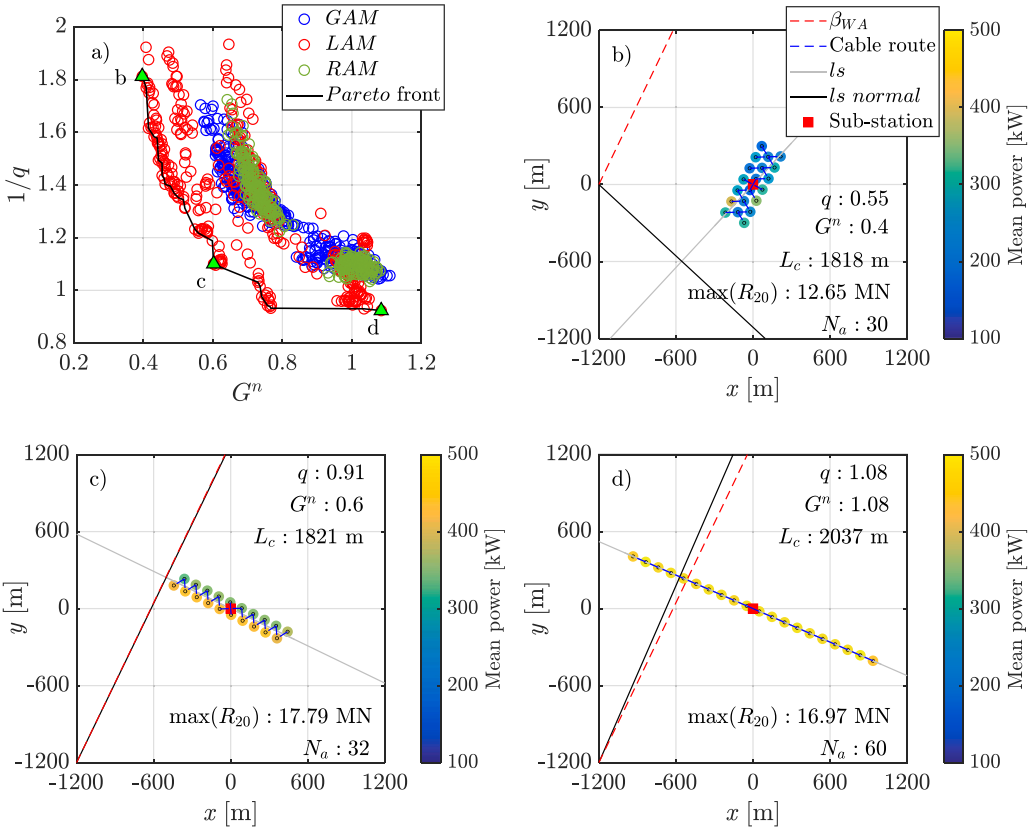

Fig. 18. As in Fig. 16 for 20 WECs.

iteration, the optimisation was repeated 3 times and similar fronts found, with minor variations in the wave farm parameters (e.g., spacing and orientation). As the inclusion of the random PTO search in the optimisation expands the range of solutions, we carried out further simulations for larger arrays including the random PTO search method.

3.3. Multi-objective optimisation for 10 and 20-WECs

To understand the array model's capabilities for an increased number of WECs, we carried out optimisation runs for 10 and 20 WECs with the three array models independently. Similar to Fig. 16, the *Pareto* fronts from each array model are extracted and post-processed to calculate G^n. The solutions from the three different models are further subjected to non-dominated sorting to identify the combined *Pareto* front for 10 WECs and 20 WECs, as shown in Figs. 17 and 18 respectively.

Unlike the 5-WEC optimisation, for 10 WECs, the *LAM* solutions populated the *Pareto* front. Although the *GAM* has an advantage of anchor sharing when WECs are present in neighbouring grid cells, due to an increased number of WECs and individual WEC evolution during each iteration, the possibility of anchor sharing for all WECs at all iterations also reduced, whereas for the *LAM,* a certain amount of anchor sharing is guaranteed due to the row arrangement. Note, for all the array models, the duration of optimisation runs was kept equal (e.g., 48 h for 10 WECs); however, due to the differences in array evolution, the number of iterations completed was slightly different for the different array models.

Similar to Fig. 16, the maximum power generating 10-WEC wave farm converged as a single row of WECs with the *ls* axis normal to β_{WA}. The wave farm close to favouring both objective functions formed two rows of WECs with a small difference between *ls* and β_{WA}. The row of WECs facing the incoming waves generated approximately 15% more power than WECs in the shadow (Fig. 17c). On the other hand, the wave farm favouring G^n formed multiple rows with *ls* nearly parallel to β_{WA}, similar to the 5-WEC optimisation (Fig. 16b). As a result of the subsequent random PTO search, the difference in power generation amongst the WECs in the farm (Fig. 17b) did not exhibit variations as smooth as seen in Fig. 17c, d.

Multi-objective optimisation for 20-WECs using three array models along with some *Pareto* candidates are shown in Fig. 18. Since similar results are obtained for 20-WEC optimisation, the discussions above are not repeated. However, in order to understand any trends in the converged solutions across different number of WECs, we computed the ratio of G^n/q for the combined *Pareto* front solutions (not shown). Minimal G^n/q can be related to the optimal trade-off solutions. Interestingly, the minimal G^n/q is obtained for the wave farm arranged in two or three rows with a small difference between the *ls* axis and β_{WA} (e.g., Fig. 17c) and (apart from the power-optimum arrays) seems to fall as the number of WECs in the array increases. Although we have no means of proving that the converged solutions are the true optimum, as our simulations resulted in consistent patterns across multiple trials and also for different numbers of WECs, we believe that the converged solutions are close to the true optimum.

4. Discussion

When comparing the wave farm layouts from all the array models, and for different numbers of WECs, the wave farms generating maximum power were mostly aligned as a single row with the *ls* axis perpendicular to the predominant wave direction. Some existing studies (e.g., Giassi and Göteman 2018, Sharp and DuPont 2018) using single-objective optimisation have also reported WECs being aligned close to a line with the *ls* axis perpendicular to the predominant wave direction for long-crested waves. Although $q > 1$ is yet to be demonstrated in the field, $q > 1$ in the linear modelling paradigm employed in the present study is plausible for the farms generating maximum power. The layouts favouring the lowest cost (G^n) objective function were mostly aligned either as 2 or 3 rows of WECs (e.g., Figs. 16b and 18b) with the *ls* axis close to parallel to the predominant wave direction. In contrast, the wave farm layouts close to favouring both objective functions were aligned as 2 rows with the converged spacing between the WEC rows (≈85 m) much smaller than the spacing between WECs (≈125 m) in each row. This is consistent for both 10 and 20 WEC arrays. Despite considering larger domains for the optimisation with different array models, the overall converged inter-device spacing ranged between 97 m and 145 m (based on multiple runs) providing insights into optimum spacing. As most of the *Pareto* front solutions in our simulations that generated maximum power were aligned perpendicular to the β_{WA}, this confirms that the wave direction is one of the key factors to be considered when designing a wave farm for maximum power generation.

For wave farms with less than 20 WECs, mooring cost accounts for a significant portion of the total capital cost (e.g., Neary et al. 2014). In the present study, due to computational limitations, a maximum farm size of 20 WECs is considered. The design loads were estimated based on a long-term probability load (Faltinsen, 1990) and thus are "passive--loads". With PTO control in addition to wave prediction at the WEC location, the maximum load may be able to be maintained within a certain limit. This may reduce the design load which in turn reduces the total capital costs. To understand the potential difference in design load, power generation and the associated mooring costs if the maximum load is capped, we carried out additional runs by capping the maximum load. For this purpose, we first estimated the short-term load (Eq. (26)) rather than the long-term load (Eq. (17)), using

$$R_{\max} = \sqrt{2\sigma_r^2 \log\left(\frac{t_s}{T_m}\right)}, \tag{26}$$

where t_s is the sea-state duration (assumed to be 3 h) and T_m is the mean wave period. Furthermore, instead of T_m, we used T_p for calculating the short-term load. This load capping method is referred to as "active-load".

For the active-load method, $R_{\max}$ is capped at 50% of max(R_{20}) of an isolated WEC. If $R_{\max} \geq 50\%$ of R_{20}, power generation for the corresponding sea state was made zero (assuming the WEC would switch to a no power generation mode). Interestingly, despite restricting the maximum load, the mean power generation was reduced by only about 12.5% compared to the mean power from the case with no maximum load. The reduction in power absorption is due to excluded sea states (as well as the probability of occurrence of the excluded sea states) that measured $R_{max} \geq 50\%$ of R_{20}. In addition, the foundation cost was calculated using Eq. (25) for the loads obtained from both active-load and passive load methods. As expected, the mooring cost was reduced (by 37%) in the active-load case compared to the passive-load case due to the reduced loads and relatively smaller foundations. This comparison was also made for some of the converged wave farm layouts from the 5 WEC optimisation and a similar result was found.

It is important to highlight some of the uncertainties associated with the methods used in this work. The load and mean power calculations adopted in this study involve several assumptions: (i) the hydrodynamic coefficients were obtained assuming linear potential theory; (ii) the PTOs were modelled as a linear spring-damper and the coefficients were optimised for the entire wave climate rather than individual sea states; (iii) the long-term load was estimated assuming Rayleigh distribution of load amplitudes; (iv) viscous drag effects were ignored and no losses were incorporated; (v) only constant flat bathymetry was considered; (vii) cylindrical buoy shape was assumed and (vi) only long-crested sea states were considered (although the sea states did have different mean directions). Uncertainties associated with some assumptions, for example, linear modelling and viscous drag effects could be quantified by conducting an experimental study or using computational fluid dynamics simulations. Our future work aims to address this using a WEC

incorporated in the non-hydrostatic model SWASH (e.g., Rijnsdorp et al. 2018). For the effects of some assumptions, we refer to existing studies. For example, the effect of different buoy shapes (e.g., sphere, ellipsoid, cylinder and chamfered cylinder) on power absorption for a different size device was investigated by Sergiienko et al. (2017) who showed that the differences were relatively small, at least for the wave conditions considered in this study. For assumptions related to directional spreading of waves, a recent study comparing the power absorption in short-crested and long-crested sea states (Göteman et al., 2018) reported only about a 1.6% variation in power absorption. Although not verified in our present work, we expect a similar conclusion.

Like all existing optimisation methodologies, computational considerations ultimately limited our ability to investigate larger arrays (in this case, >20 WECs). Although the use of a semi-analytical approach to obtain the hydrodynamic coefficients reduces computation time compared to boundary element methods, it is still computationally demanding. For example, for a 20-WEC array, it took 72 h to complete 50 iterations on a supercomputer (our simulations utilized the Magnus system at the Pawsey Supercomputing Centre in Western Australia) with 24 cores. Reducing computational time for a larger number of devices can make use of methods previously published in the literature such as the Fast Multipole Algorithm (Borgarino et al., 2012) or by neglecting the scattered waves (Göteman et al., 2015). In the present work, we did not explore any strategies to reduce computational time; this will be considered in future work.

5. Conclusions

In this paper, a probability-based evolutionary multi-objective optimisation framework for submerged wave farms has been developed. The focus in demonstrating this method was on four objective functions including power generation, design load, number of anchors and length of transmission cables, with the latter three being large costs in the construction of a wave farm. Multi-objective optimisation allows optimisation to be completed without knowing the weighting that should be applied to each objective. As a result, the collection of non-dominated solutions can be used to quickly find new optimal solutions in the event that a weighting changes (for example, the anchor type, cost of cable installation, etc.). In this work, an example cost model, which assigns specific weightings to the objective function values, was presented to illustrate how optimal solutions could be further narrowed down in decision making. Results in the objective space have been presented to weigh the cost against power production for a range of array layouts. Multi-objective optimisation runs were carried out for different numbers of WECs (5, 10 and 20) with three different array models (grid array, linear array and random array) using site-specific wave conditions.

Optimisation results showed that the converged layouts in the combined *Pareto* optimal front (from all three array approaches) favouring maximum power generation were mostly aligned as a single row of WECs. The least-square axis of these layouts was close to perpendicular to the predominant wave direction (e.g., Fig. 16d) and was consistent for 10 and 20 WECs (e.g., Figs. 17d, 18d). This finding agreed with existing optimisation studies where maximising power absorption was used as the single objective (Giassi and Göteman, 2018; Neshat et al., 2020; Tokić and Yue, 2021). The three array models performed similarly with a small number of WECs (5). However, with an increasing number of WECs, the linear array appears to outperform both grid and random array models (based on the duration of simulations considered in this study). We also found a consistent pattern in the optimal wave farm layouts as the number of WECs was increased (Figs. 16–18). In this work, the presence of multiple objectives (with objectives competing with each other) results in optimal layouts not forming a single line, depending on the relative importance of the objectives (Fig. 17b, c). This approach offers insight into cost versus revenue in the frame of competing objectives, which is important when designing arrays with minimal LCoE (as opposed to arrays maximising power absorption). While we did not develop an LCoE model, the method can be easily extended to rank the optimum solutions according to their LCoE if a full cost model is known.

The multi-objective optimisation tool developed and tested here has the potential to be applied to a different class of WEC farms with different working principles. Furthermore, the outcome of this study is likely also transferable to similar classes (point absorbers) of WECs with similar working principles. Considering the complexity of the problem, the framework developed in this study can be beneficial and will be of practical aid in designing wave energy farms using more comprehensive and likely conflicting objective functions.

CRediT authorship contribution statement

Daniel R. David: Conceptualization, Methodology, Formal analysis, Visualization, Writing – original draft, Writing – review & editing. **Adi Kurniawan:** Conceptualization, Methodology, Writing – original draft, Writing – review & editing, Supervision. **Hugh Wolgamot:** Conceptualization, Methodology, Writing – original draft, Writing – review & editing, Supervision. **Jeff E. Hansen:** Conceptualization, Methodology, Writing – original draft, Writing – review & editing, Funding acquisition, Supervision. **Dirk Rijnsdorp:** Writing – original draft, Writing – review & editing, Supervision. **Ryan Lowe:** Writing – original draft, Writing – review & editing, Funding acquisition, Supervision.

Declaration of Competing Interest

The authors declare that they have no known competing financial interests or personal relationships that could have appeared to influence the work reported in this paper.

Acknowledgements

This project forms part of a Ph.D. study by D.R.D at the University of Western Australia which is supported by the Commonwealth Government through an Australian Government Research Training Program Scholarship. Funding was provided by the Australian Renewable Energy Agency, Research and Development Programme (grant number 2015RND086 in partnership with Carnegie Clean Energy) and the Wave Energy Research Centre (through funding provided by the Western Australian Government, via the Department of Primary Industries and Regional Development (DPIRD), and the University of Western Australia). Supercomputer access was provided by the Pawsey Supercomputing Centre with funding from the Australian Government and the Government of Western Australia. HW is supported by an Australian Research Council (ARC) Early Career Fellowship (DE200101478). We thank Christophe Gaudin, Jana Orszaghova, Guy McCauley, Michael Cuttler, Matt Hatcher, Mario Conde, Renan Fonseca da Silva and Yongmin Cai for fruitful discussions that benefitted this work. We greatly appreciate the time and effort of three anonymous reviewers whose feedback improved this paper.

Appendix A. Cost model

To find the total cost related to the objective functions considered in this work, we followed a method similar to Gaudin et al. (2021). For the foundation, we first designed a pile based on the R_{20} estimate (Section 2.5) of each tether. The pile diameter (P_D) was fixed as 4 m and the pile wall

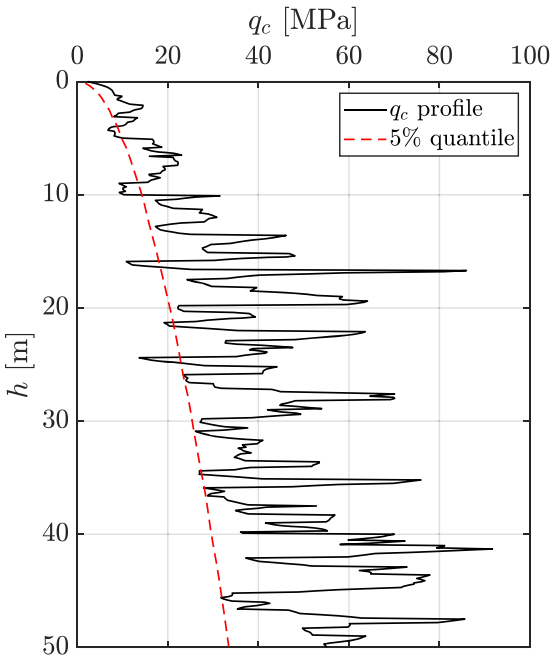

Fig. A.1. Cone tip resistance, q_c, profile based on the random field theory.

thickness was fixed as 0.08 m, hence the pile length (P_L) was the only variable to calculate to fulfil the axial capacity requirements. The cone tip resistance profile (q_c) for a representative seabed condition (Fig. A.1) was adopted from Cai et al. (2021), which is based on random field theory. We utilized the UWA-05 method (Lehane et al., 2007) to calculate the axial capacity factor of the open-ended pile, where the R_{20} estimate of each tether was fixed as the design load for each pile:

$$R_{20}\left[\frac{q_c(5\%)}{\gamma_m}\right] = \pi P_D \int_0^{P_L} \tau_f \mathrm{dz} \tag{A.1}$$

$$\tau_f = 0.0225\frac{q_c(5\%)}{\gamma_m}\tan\delta_f\left[1-\min\left(1,(P_D/1.5)^{0.2}\right)(P_{Di}/P_D)^2\right]^{0.3}\left[\max(h_t/P_D,2)\right]^{-0.5} \tag{A.2}$$

Here, τ_f is the local shaft friction, γ_m is the material factor (fixed as 1.25), h_t is the height above the pile tip and P_{Di} is the inner diameter of the pile. The constant volume interface angle (δ_f) was fixed as 29°.

Once the length of the pile is determined, the pile manufacturing cost ($cost_{pm}$) is approximated based on (refer to Gaudin et al. (2021) for more details)

$$cost_{pm} = \alpha_f cost_{st} w_{\text{steel}}, \tag{A.3}$$

where α_f (=1.2) is the pile fabrication factor, $cost_{st}$ (=$3500/tonne, all cost in US dollars) is the steel unit cost and w_{steel} is the total steel weight in tonnes.

In order to account for the number of foundations in the cost model, we calculated the pile installation cost as

$$cost_{pi} = cost_{\text{vessel}} T_{\text{install}} \alpha_i, \tag{A.4}$$

$$T_{\text{install}} = T_{pp} + \frac{T_{pd}(sec)}{(3600\times 24)}, \tag{A.5}$$

$$T_{pd} = N_{\text{blow}} P_L T_{\text{hammer}}, \tag{A.6}$$

where $cost_{pi}$ is the installation cost per pile, $cost_{\text{vessel}}$ is the vessel operation day rate (= $200,000/day), T_{install} is the installation duration (in days) of each pile, α_i is the installation downtime/contingency factor fixed as 1.2, T_{pp} is the preparation duration for each pile fixed as 0.33 day, T_{pd} is the driving duration (in seconds) for each pile, N_{blow} is the number of driving blows for per metre penetration (fixed as 85) and T_{hammer} is the hammer blow period fixed as 6 s/blow.

Depending on the number of foundations, the cost of mobilisation may increase or decrease and might influence the total cost. For simplicity, the mobilisation costs are not considered here. To further simplify the cost model, we considered a range of loads from 5 to 25 MN and calculated the costs associated with foundation ($cost_f = cost_{pm} + cost_{pi}$) for each load. Using linear regression, the cost associated with foundation is reduced into

$$cost_f = \left(5.65\times 10^4\right)R_{20} + 2.9\times 10^5. \tag{A.7}$$

Similar to Gaudin et al. (2021), the cost of electrical cable connecting all WECs in the array was fixed as $400/m and the cost of the export cable from the sub-station to a grid connection (= 1500 m) was fixed as $3000/m. Adding the cable cost to Eq. A.7, we obtained the total cost (Eq. (25)) related to the objective functions considered in this work as

$$G = \sum_{i}^{N_a}\left(\left(5.65\times10^{4}\right)R_{20,i}+2.9\times10^{5}\right)+\left(0.4\times10^{3}\right)L_c+4.5\times10^{6}, \tag{A.8}$$

where N_a is the total number of foundations in an array and L_c is the length of the cable connecting each WEC in the array.

Note, that the cost of individual components is highly volatile and varies significantly between countries, at different times, amongst other factors. We compared our costs with some of the existing literature and found similarities and differences. For example, the vessel day rate was found to be in the range reported in the literature (e.g., Ahn et al. 2017, Jiang 2021). However, the cost of cable and steel was found to differ compared to existing literature (Giassi et al., 2020; Neary et al., 2014; Nieradzinska et al., 2016). A maximum difference of about 30% was observed, however, this is not entirely unexpected due to the cost of cable varying with the type and capacity and the variability in steel pricing by location and through time.

References

Ahn, D., Shin, S.C., Kim, S.Y., Kharoufi, H., Kim, H.C., 2017. Comparative evaluation of different offshore wind turbine installation vessels for Korean west–south wind farm. Int. J. Nav. Archit. Ocean Eng. 9, 45–54. https://doi.org/10.1016/j.ijnaoe.2016.07.004.

Arbonès, D.R., Ding, B., Sergiienko, N.Y., Wagner, M., 2016. Fast and effective multi-objective optimisation of submerged wave energy converters. In: Proceedings of the parallel problem solving from nature – PPSN XIV, pp. 675–685. https://doi.org/10.1007/978-3-319-45823-6_63 eds J. Handl, E. Hart, P. R. Lewis, M. López-Ibáñez, G. Ochoa, B. Paechter (Edinburgh Springer Int. Publ. 9921 LNCS.

Arbonès, D.R., Sergiienko, N.Y., Ding, B., Krause, O., Igel, C., Wagner, M., 2018. Sparse incomplete LU-decomposition for wave farm designs under realistic conditions. In: Proceedings of the parallel problem solving from nature – PPSN XV, pp. 512–524. https://doi.org/10.1007/978-3-319-99253-2_41 eds A. Auger, C. M. Fonseca, N. Lourenço, P. Machado, L. Paquete, D. Whitley (Coimbra Springer Int. Publ. 11101 LNCS.

Babarit, A., 2013. On the park effect in arrays of oscillating wave energy converters. Renew. Energy 58, 68–78. https://doi.org/10.1016/j.renene.2013.03.008.

Babarit, A., Hals, J., Muliawan, M.J., Kurniawan, A., Moan, T., Krokstad, J., 2012. Numerical benchmarking study of a selection of wave energy converters. Renew. Energy 41, 44–63. https://doi.org/10.1016/j.renene.2011.10.002.

Birk, L., 2009. Application of constrained multi-objective optimization to the design of offshore structure hulls. J. Offshore Mech. Arct. Eng. 131, 1–9. https://doi.org/10.1115/1.2957919.

Borgarino, B., Babarit, A., Ferrant, P., 2012. Impact of wave interactions effects on energy absorption in large arrays of wave energy converters. Ocean Eng. 41, 79–88. https://doi.org/10.1016/j.oceaneng.2011.12.025.

Budal, K., 1977. Theory for absorption of wave power by a system of interacting bodies. J. Ship Res. 21, 248–253. https://doi.org/10.5957/jsr.1977.21.4.248.

Cai, Y., Bransby, F., Gaudin, C., Uzielli, M., 2021. A framework for the design of vertically loaded piles in spatially variable soil. Comput. Geotech. 134, 104140 https://doi.org/10.1016/j.compgeo.2021.104140.

Child, B.F.M., Venugopal, V., 2010. Optimal configurations of wave energy device arrays. Ocean Eng. 37, 1402–1417. https://doi.org/10.1016/j.oceaneng.2010.06.010.

Cuttler, M.V.W., Hansen, J.E., Lowe, R.J., 2020. Seasonal and interannual variability of the wave climate at a wave energy hotspot off the southwestern coast of Australia. Renew. Energy 146, 2337–2350. https://doi.org/10.1016/j.renene.2019.08.058.

De Andres, A., Medina-Lopez, E., Crooks, D., Roberts, O., Jeffrey, H., 2017. On the reversed LCoE calculation: design constraints for wave energy commercialization. Int. J. Mar. Energy 18, 88–108. https://doi.org/10.1016/j.ijome.2017.03.008.

Deb, K., 2011. Multi-objective optimisation using evolutionary algorithms: an introduction. Multi-Objective Evolutionary Optimisation for Product Design and Manufacturing. Springer London, London. https://doi.org/10.1007/978-0-85729-652-8_1.

Deb, K., Agrawal, S., Pratap, A., Meyarivan, T., et al., 2000. A fast elitist non-dominated sorting genetic algorithm for multi-objective optimization: NSGA-II. In: Schoenauer, M., Deb, K., Rudolph, G., Yao, X., Lutton, E., Merelo, J.J., et al. (Eds.), Parallel Problem Solving from Nature PPSN VI. Springer Berlin Heidelberg, Berlin, Heidelberg, pp. 849–858.

Evans, D.V., 1980. Some analytic results for two and three dimensional wave-energy absorbers. In: Count, B.M. (Ed.), Power From Sea Waves. Academic Press, Edinburgh, pp. 213–249.

Falnes, J., 2002. Ocean Waves and Oscillating Systems: Linear Interaction Including Wave Energy Extraction. Cambridge Univ. Press, Cambridge, UK. https://doi.org/10.1007/s13398-014-0173-7.2.

Falnes, J., 1980. Radiation impedance matrix and optimum power absorption for interacting oscillators in surface waves. Appl. Ocean Res. 2, 75–80. https://doi.org/10.1016/0141-1187(80)90032-2.

Falnes, J., Budal, K., 1982. Wave-power absorption by parallel rows of interacting oscillating bodies. Appl. Ocean Res. 4, 194–207. https://doi.org/10.1016/S0141-1187(82)80026-6.

Faltinsen, O.M., 1990. Sea Loads On Ships and Offshore Structures. Cambridge University press, 9780521458702.

Fitzgerald, C., Thomas, G., 2016. A preliminary study on the optimal formation of an array of wave power devices. J. Theor. Appl. Mech. 53, 411–421. https://doi.org/10.15632/jtam-pl.54.2.411.

Fox, A.D., Corne, D.W., Mayorga Adame, C.G., Polton, J.A., Henry, L.A., Roberts, J.M., 2019. An efficient multi-objective optimization method for use in the design of marine protected area networks. Front. Mar. Sci. 6, 1–15. https://doi.org/10.3389/fmars.2019.00017.

Gaudin, C., David, D.R., Cai, Y., Hansen, J.E., Bransby, F., Rijnsdorp, D.P., Lowe, R.J., O'Loughlin, C., Lu, T., O'Neill, M., 2021. From single to multiple wave energy converters: Cost reduction through location and configuration optimisation, Final Report, The University of Western Australia. https://arena.gov.au/assets/2021/10/wave-energy-cost-reduction-resource-assessment-report.pdf.

Ghasemian, S., Faridzad, A., Abbaszadeh, P., Taklif, A., Ghasemi, A., Hafezi, R., 2020. An overview of global energy scenarios by 2040: identifying the driving forces using cross-impact analysis method. Int. J. Environ. Sci. Technol. https://doi.org/10.1007/s13762-020-02738-5.

Giassi, M., Castellucci, V., Göteman, M., 2020. Economical layout optimization of wave energy parks clustered in electrical subsystems. Appl. Ocean Res. 101, 102274 https://doi.org/10.1016/j.apor.2020.102274.

Giassi, M., Göteman, M., 2018. Layout design of wave energy parks by a genetic algorithm. Ocean Eng. 154, 252–261. https://doi.org/10.1016/j.oceaneng.2018.01.096.

Göteman, M., Engström, J., Eriksson, M., Isberg, J., 2015. Optimizing wave energy parks with over 1000 interacting point-absorbers using an approximate analytical method. Int. J. Mar. Energy 10, 113–126. https://doi.org/10.1016/j.ijome.2015.02.001.

Göteman, M., Giassi, M., Engström, J., Isberg, J., 2020. Advances and challenges in wave energy park optimization-a review. Front. Energy Res. 8 https://doi.org/10.3389/fenrg.2020.00026.

Göteman, M., McNatt, C., Giassi, M., Engström, J., Isberg, J., 2018. Arrays of point-absorbing wave energy converters in short-crested irregular waves. Energies 11, 964. https://doi.org/10.3390/en11040964.

Jiang, Z., 2021. Installation of offshore wind turbines: a technical review. Renew. Sustain. Energy Rev. 139, 110576 https://doi.org/10.1016/j.rser.2020.110576.

Kagemoto, H., Yue, D.K.P., 1986. Interactions among multiple three-dimensional bodies in water waves: an exact algebraic method. J. Fluid Mech. 166, 189–209.

Karimi, M., Hall, M., Buckham, B., Crawford, C., 2017. A multi-objective design optimization approach for floating offshore wind turbine support structures. J. Ocean Eng. Mar. Energy 3, 69–87. https://doi.org/10.1007/s40722-016-0072-4.

Koumousis, V.K., Katsaras, C.P., 2006. A saw-tooth genetic algorithm combining the effects of variable population size and reinitialization to enhance performance. IEEE Trans. Evol. Comput. 10, 19–28. https://doi.org/10.1109/TEVC.2005.860765.

Kurniawan, A., Ma, G., 2009. Optimization of ballast plan in launch jacket load-out. Struct. Multidiscip. Optim. 38, 267–288. https://doi.org/10.1007/s00158-008-0287-7.

Kurniawan, A., Moan, T., 2013. Optimal geometries for wave absorbers oscillating about a fixed axis. IEEE J. Ocean. Eng. 38, 117–130. https://doi.org/10.1109/JOE.2012.2208666.

Lehane, B.M., Schneider, J.A., Xu, X., 2007. Development of the UWA-05 design method for open and closed ended driven piles in siliceous sand 40902, 1–10. 10.1061/40902(221)12.

Lobo, F.G., Goldberg, D.E., 2004. The parameter-less genetic algorithm in practice. Inf. Sci. 167, 217–232. https://doi.org/10.1016/j.ins.2003.03.029 (Ny).

López-Ruiz, A., Bergillos, R.J., Raffo-Caballero, J.M., Ortega-Sánchez, M., 2018. Towards an optimum design of wave energy converter arrays through an integrated approach of life cycle performance and operational capacity. Appl. Energy 209, 20–32. https://doi.org/10.1016/j.apenergy.2017.10.062.

Mahrach, M., Miranda, G., León, C., Segredo, E., 2020. Comparison between single and multi-objective evolutionary algorithms to solve the knapsack problem and the travelling salesman problem. Mathematics 8, 1–23. https://doi.org/10.3390/math8112018.

McCauley, G., Wolgamot, H., Orszaghova, J., Draper, S., 2018. Linear hydrodynamic modelling of arrays of submerged oscillating cylinders. Appl. Ocean Res. 81, 1–14. https://doi.org/10.1016/j.apor.2018.09.012.

McIver, P., 1994. Some hydrodynamic aspects of arrays of wave-energy devices. Appl. Ocean Res. 16, 61–69. https://doi.org/10.1016/0141-1187(94)90003-5.

Mercadé Ruiz, P., Nava, V., Topper, M.B.R., Minguela, P.R., Ferri, F., Kofoed, J.P., 2017. Layout optimisation of wave energy converter arrays. Energies 10. https://doi.org/10.3390/en10091262.

Neary, V.S., Previsic, M., Jepsen, R.A., Lawson, M.J., Yu, Y.-.H., Copping, A.E., Fontaine, A.A., Hallett, K.C., Murray, D.K., 2014. Methodology for Design and Economic Analysis of Marine Energy Conversion (MEC) Technologies, 261. Sandia Natl. Lab.

Neshat, M., Alexander, B., Wagner, M., 2020. A hybrid cooperative co-evolution algorithm framework for optimising power take off and placements of wave energy converters. Inf. Sci. 534, 218–244. https://doi.org/10.1016/j.ins.2020.03.112 (Ny).

Nieradzinska, K., MacIver, C., Gill, S., Agnew, G.A., Anaya-Lara, O., Bell, K.R.W., 2016. Optioneering analysis for connecting Dogger Bank offshore wind farms to the GB electricity network. Renew. Energy 91, 120–129. https://doi.org/10.1016/j.renene.2016.01.043.

Orszaghova, J., Wolgamot, H., Draper, S., Taylor, P.H., Rafiee, A., 2020. Onset and limiting amplitude of yaw instability of a submerged three-tethered buoy. Proc. R. Soc. A Math. Phys. Eng. Sci. https://doi.org/10.1098/rspa.2019.0762.

Pelikan, M., Goldberg, D.E., Cantú-Paz, E., 2000. Bayesian optimization algorithm, population sizing, and time to convergence. In: Proceedings of the genetic and evolutionary computation conference, pp. 275–282.

Prim, R.C., 1957. Shortest connection networks and some generalizations. Bell Syst. Tech. J. 36, 1389–1401. https://doi.org/10.1002/j.1538-7305.1957.tb01515.x.

Rijnsdorp, D.P., Hansen, J.E., Lowe, R.J., 2018. Simulating the wave-induced response of a submerged wave-energy converter using a non-hydrostatic wave-flow model. Coast. Eng. https://doi.org/10.1016/j.coastaleng.2018.07.004.

Rodrigues, S., Bauer, P., Bosman, P.A.N., 2016. Multi-objective optimization of wind farm layouts – complexity, constraint handling and scalability. Renew. Sustain. Energy Rev. 65, 587–609. https://doi.org/10.1016/j.rser.2016.07.021.

Roeva, O., Fidanova, S., Paprzycki, M., 2013. Influence of the population size on the genetic algorithm performance in case of cultivation process modelling. In: Proceedings of the federated conference on computer science and information systems (FedCSIS), 2013, pp. 371–376.

Schulze-Riegert, R., Krosche, M., Fahimuddin, A., Ghedan, S., 2007. Multiobjective optimization with application to model validation and uncertainty quantification. Proceedings of the SPE middle east oil gas show MEOS 2, 827–833. https://doi.org/10.2118/105313-ms.

Sergiienko, N.Y., Cazzolato, B.S., Ding, B., Hardy, P., Arjomandi, M., 2017. Performance comparison of the floating and fully submerged quasi-point absorber wave energy converters. Renew. Energy 108, 425–437. https://doi.org/10.1016/j.renene.2017.03.002.

Sergiienko, N.Y., Rafiee, A., Cazzolato, B.S., Ding, B., Arjomandi, M., 2018. Feasibility study of the three-tether axisymmetric wave energy converter. Ocean Eng. 150, 221–233. https://doi.org/10.1016/j.oceaneng.2017.12.055.

Sharp, C., DuPont, B., 2018. Wave energy converter array optimization: a genetic algorithm approach and minimum separation distance study. Ocean Eng. 163, 148–156. https://doi.org/10.1016/j.oceaneng.2018.05.071.

The Mathworks, Inc. MATLAB, Version 9.6, 2019, 2019. MATLAB 2019b - MathWorks. Www.Mathworks.Com/Products/Matlab.

Thomas, G.P., Evans, D.V., 1981. Arrays of three-dimensional wave-energy absorbers. J. Fluid Mech. 108, 67–88.

Tokić, G., Yue, D.K.P., 2021. Hydrodynamics of large wave energy converter arrays with random configuration variations. J. Fluid Mech. 923, 1–12. https://doi.org/10.1017/jfm.2021.584.

Weller, S.D., Stallard, T.J., Stansby, P.K., 2010. Experimental measurements of irregular wave interaction factors in closely spaced arrays. IET Renew. Power Gener. 4, 628–637. https://doi.org/10.1049/iet-rpg.2009.0192.

Wolgamot, H.A., Taylor, P.H., Eatock Taylor, R., 2012. The interaction factor and directionality in wave energy arrays. Ocean Eng. 47, 65–73. https://doi.org/10.1016/j.oceaneng.2012.03.017.

Zakaria, M.Z., Jamaluddin, H., Ahmad, R., Loghmanian, S.M., 2012. Comparison between multi-objective and single-objective optimization for the modeling of dynamic systems. Proc. Inst. Mech. Eng. Part I J. Syst. Control Eng. 226, 994–1005. https://doi.org/10.1177/0959651812439969.

Zhong, Q., Yeung, R.W., 2019. Model-predictive control strategy for an array of wave-energy converters. J. Mar. Sci. Appl. 18, 26–37. https://doi.org/10.1007/s11804-019-00081-x.